

1 The distribution and evolution of supraglacial lakes on the 79 °N 2 Glacier (northeast Greenland) and interannual climatic controls

3
4 Jenny V. Turton¹., Philipp Hochreuther¹., Nathalie Reimann¹., Manuel T. Blau^{2,3}

5 ¹Institute of Geography, Friedrich-Alexander University, 90154 Erlangen, Germany

6 ²Department of Climate System, Pusan National University, Busan 46241, South Korea

7 ³Centre for Climate Physics, Institute for Basic Science, Busan 46241, South Korea

8
9 *Correspondence to:* Jenny V. Turton (jenny.turton@fau.de)

10
11 **Abstract.** The Nioghalvfjærdssjorden glacier (also known as 79 North Glacier) drains approximately 8% of the
12 Greenland ice sheet. Supraglacial lakes (SGLs), or surface melt ponds, are a persistent summertime feature, and are
13 thought to drain rapidly to the base of the glacier and influence seasonal ice velocity. However, seasonal development
14 and spatial distribution of SGLs in the northeast of Greenland is poorly understood, leaving a substantial error on the
15 estimate of melt water and its impacts on ice velocity. Using results from an automated detection of melt ponds,
16 atmospheric and surface mass balance modelling and reanalysis products, we investigate the role of specific climatic
17 conditions on melt onset, extent and duration from 2016 to 2019. The summers of 2016 and 2019 were characterised by
18 above average air temperatures, particularly in June, as well as a number of rainfall events, which led to extensive melt
19 ponds to elevations up to 1600 m. Conversely, 2018 was particularly cold, with a large accumulated snowpack, which
20 limited the development of lakes to altitudes less than 800 m. There is evidence of inland expansion and increases in the
21 total area of lakes compared to the early 2000s, as projected by future global warming scenarios.

22 23 1 Introduction

24 Nioghalvfjærdssjorden, also known as 79° North Glacier (henceforth 79 °N glacier) is a marine-terminating glacier on
25 the northeast coast of Greenland. Approximately 8 % of the Greenland Ice Stream (GIS) drains into 79 °N through the
26 North East Greenland Ice Stream (NEGIS), making it the largest discharger of ice in northern Greenland (Mouignot et
27 al. 2015, Mayer et al. 2018). Prior to the 21st century, NEGIS, which extends 600 km into the interior of the GIS
28 (Figure 1), was believed to be stable, with little change in ice dynamics (Khan et al. 2014, Mayer et al. 2018).
29 However, since 2006 NEGIS has undergone pronounced thinning of 1 m year⁻¹, and the floating tongue of 79 °N has
30 retreated by 2-3 km since 2009 (Khan et al. 2014). Recently, over 100 km² of ice was lost through calving of a tributary
31 glacier to 79 °N, Spalte Glacier (Figure S1), following record-breaking summer air temperatures in 2019 and 2020,
32 highlighting the vulnerability of this region to climate change and surface melt.

33 The surface of 79 °N and the NEGIS feature persistent melt water ponds, or Supraglacial Lakes (SGL), and
34 meltwater drainage channels (Figure S1). SGLs are a frequent summertime feature on many glaciers in Greenland (Pope
35 et al 2016), on ice shelves (e.g Larsen C; Luckman et al 2014) and on sea ice (Perovich et al 2002). The albedo of SGLs
36 is between 0.1 and 0.6, depending on their depth (Malinka et al 2018), and therefore they absorb much more shortwave
37 radiation than the surrounding solid ice (Buzzard et al 2018a). SGLs influence both the Surface Mass Balance (SMB)
38 and the dynamical stability of glaciers through lowering the albedo at the surface and draining water to the base, which
39 reduces friction and influences ice flow velocity (Zwally et al. 2002; Vijay et al. 2019). Both ice velocity increases and
40 decreases have been linked to the drainage of SGLs across Greenland. Short-lived velocity increases have been
41 observed during summer in several marine-terminating glaciers, including 79 °N Glacier (Rathmann et al 2017). Both

42 Rathmann et al (2017) and Vijay et al (2019) hypothesise that the summer speed-up of 79 °N Glacier occurs when
43 SGLs drain to the base and alter the subglacial hydrology. Conversely, on land-terminating glaciers, SGL drainage has
44 been shown to reduce ice velocity in the seasonal to decadal time scales (Sundal et al. 2011; Tedstone et al. 2015).
45 SGLs are a key component of the SMB and yet rarely feature in mass balance models or estimates (Smith et al. 2017,
46 Yang et al. 2019). Despite the high number of studies focusing on surface mass loss from the Greenland Ice sheet (e.g
47 Lüthje et al. 2006, Das et al. 2008, Tedesco et al. 2012, Stevens et al. 2015), the relationship between SMB, run-off and
48 SGL development remains unclear.

49 Despite the widespread occurrence of SGLs, very few studies have investigated the relationship between the
50 seasonal evolution of SGLs and the atmospheric processes required for their formation in this region. Previous studies
51 have largely focused on Antarctic ice shelves (Langley et al. 2016, Arthur et al. 2020, Leeson et al. 2020) and southern
52 and western Greenland (Lüthje et al. 2006, Das et al. 2008, Tedesco et al. 2012, Stevens et al. 2015). Recently, more
53 northerly locations have been investigated, including Petermann Glacier (Macdonald et al. 2018). Multispectral satellite
54 products now provide observations of SGL over northeast Greenland at both high-temporal and -spatial resolution, and
55 in many cases free of charge. The northeast of Greenland, and specifically the NEGIS region, has, until recently, lacked
56 such detailed analysis of SGLs, however, this region is likely to show an inland expansion of SGL and ablation zone in
57 the near future (Leeson et al. 2015; Igneczi et al. 2016; Noël et al. 2019). Sundal et al. (2009) used MODIS data to
58 assess the lake area between 2003 and 2007 for 79 °N Glacier amongst other locations. However, as the ASTER images
59 were acquired at a later stage in the melt season, the percentage of unidentified lake area at the start of the summer is
60 likely to be higher than 12 % (Sundal et al. 2009). Winter estimates of liquid water area on the 79 °N Glacier are also
61 now available from Schröder et al. (2020). Recently, Hochreuther et al. (2021) developed an automated melt detection
62 algorithm for Sentinel-2 satellite data. This provides a near-daily, ~~very high 10 m spatial resolution (10m)~~ time series of
63 SGLs on NEGIS during summertime.

64 Widespread summer melting was observed over Greenland in 2007, 2010 and 2012, ~~which prompted research~~
65 ~~into large-scale~~ teleconnection patterns (Tedesco et al. 2013, Lim et al. 2016, Hanna et al. 2014a). ~~These patterns of~~
66 ~~atmospheric variability have been found to influence the air temperature and precipitation in Greenland.~~ The North
67 Atlantic Oscillation (often termed NAO) is the dominant mode of variability for Greenland and the Arctic, defined as
68 the 'seesaw' of atmospheric surface pressure changes between Iceland and the Azores (Hildebrandsson 1897, Hanna et
69 al 2014b). Three other modes of atmospheric variability were found to be important for specifically the northeast and
70 east of Greenland by Lim et al (2016): the Arctic Oscillation, the East Atlantic pattern, and the Greenland Blocking
71 ~~Index~~. Generally (for the whole of Greenland), a negative phase of the North Atlantic Oscillation and Arctic Oscillation
72 are associated with a warm and dry atmosphere over the GIS, and often leads to mass loss at the surface (Lim et al
73 2016). Furthermore, a positive Greenland Blocking Index (especially when combined with a positive East Atlantic
74 pattern and negative North Atlantic Oscillation index) also leads to positive temperature anomalies over the GIS.

75 ~~Extreme Greenland-wide melt seasons, such as in 2012, have been linked to specific teleconnection patterns (Tedesco et~~
76 ~~al. 2013), however no studies have assessed the potential role of teleconnections on the development of SGLs or~~
77 ~~localised melt conditions.~~

78 ~~Along with large-scale teleconnection influences, smaller-scale mesoscale processes also influence the climate~~
79 ~~and melting over Greenland. Recently, atmospheric rivers, or narrow filament-like regions of intense water vapour~~
80 transport in the atmosphere, have been investigated in response to extreme surface mass balance variations in the
81 northwest of Greenland (Bonne et al. 2015; Mattingly et al. 2018; 2020). In most cases, the northeast of Greenland,
82 especially the coastal regions and marine-terminating glaciers, have received little or no attention during ~~extreme~~
83 ~~melting~~ years, possibly due to weaker teleconnection signals (Lim et al. 2016) or due to low spatial resolution data

Formatted: Strikethrough

Formatted: Font colour: Red

Formatted: Strikethrough

Formatted: Font colour: Red

Deleted: due to particularly warm summers and specific

Formatted: Font colour: Red

Deleted: Index .

Formatted: Font colour: Red

Formatted: Font colour: Red

Formatted: Font colour: Red

Deleted: ¶

Deleted: More r

Deleted: these stand-out

Formatted: Font colour: Red

89 (Oltmanns et al. 2019). Similarly, prior to the mid 2010's, the majority of melting was located in the southern and
90 western parts of Greenland, leading to vast research for these regions (e.g van de Wal et al. 2005; 2012; Tedstone et al.
91 2017; Kuipers Munneke et al. 2018). However, after the mid 2010's, the highest melt anomalies were located in
92 northern Greenland, especially in 2014 and 2016 (Tedesco et al. 2016). Recently, a low-permeability ice slab was
93 identified in northeast Greenland and within 79 °N Glacier (MacFerrin et al. 2019). The meters-thick, englacial layers
94 of refrozen melt water enhance melting and runoff processes and are sustained with relatively small amounts of melt
95 water from drainage of SGLs (MacFerrin et al. 2019). With a warming climate, it is likely that the ice slabs will become
96 more widespread and persistent, although more research is required to investigate the glacio-hydrology in these regions.
97 In a recent review paper, Flowers (2018) highlighted that further investigation into surface melt water volume, drainage
98 and runoff from marine-terminating glaciers is required.

99 The specific aims of this study are to investigate: 1) the spatial distribution of SGLs over the 79 °N glacier, 2)
100 the life-cycle of lake development, 3) the atmospheric and topographic controls on melt pond evolution in the northeast
101 of Greenland between 2016 and 2019 and 4) whether and how conditions have changed since the Sundal et al. (2009)
102 study in the early 2000s. To accomplish this, we use a combination of ~~very high-resolution (10m)~~ Sentinel-2 data, high-
103 resolution (1 km) atmospheric modelling output from the Polar Weather Research and Forecasting (PWRF) model and
104 surface mass balance estimates from the COSIPY model, as well as in-situ observations.

105 In Section 2, we introduce the automatic detection algorithm and data used in the study, followed by the results
106 (Section 3). These are separated into topographic (Section 3.2) and climatic (Section 3.3) controls of the SGL formation
107 and spatial distribution. The discussion continues in Section 4 and the research concludes in Section 5.

109 2 Data and Methods

110 2.1 Automated SGL detection algorithm

111 Automatic SGL detection algorithms have previously been applied to a number of satellite records including MODIS
112 (Sundal et al. 2009), Landsat8 (Williamson et al. 2018), Sentinel-1 (Schröder et al. 2020) and Sentinel-2 (Williamson et
113 al. 2018; Hochreuther et al. 2021). A previously developed SGL detection algorithm by Hochreuther et al (2021) has
114 been applied to Sentinel-2 data between March and September 2016-2019 for melt pond tracking. For a full description
115 of the processes involved in SGL detection, see Hochreuther et al. (2021), however a brief overview is provided here.

116 ~~High resolution (10-60m)~~ Optical imagery is collected from two twin satellites, Sentinel-2 A and B, at a revisit duration
117 of approximately 1-2 days at this latitude ~~and a spatial resolution between 10 and 60 m~~. Whilst launched in 2015, data
118 coverage was too low over the study area to extract a meaningful timeseries of SGLs. Therefore, the timeseries used
119 here runs from March 29, 2016 to September 19, 2019.

120 An empirically developed and locally tuned static band ratio threshold for the blue to red band spectra was
121 applied. This approach was chosen over the often-applied NDWI due to faster computation and expected similar results
122 (Williamson et al. 2017; Hochreuther et al. 2021). To delineate ice and slush from liquid water, thresholds between 1.0
123 and 2.4 were tested and compared visually to true colour images, resulting in a best fit at a ratio of 1.6. After the
124 application of the threshold, the images were cropped to the grounded ice. The GIMP land classification map (Howat et
125 al. 2014), updated by a Sentinel 2-image from 2016 and combined with an ERS-2 SAR-based grounding line estimation
126 was used to delineate the eastern ice margin (Hochreuther et al. 2021). Sieving the binary mask, again with iterative size
127 testing in ~~advance, reduced~~ noise stemming from crevasse- and serac fields, retaining only water areas larger than 150
128 pixels (0.015 km²). This potentially causes a number of very small lakes being ~~missed but~~ represents the best possible
129 compromise between falsely removing small lakes and falsely retaining misclassifications due to shadows or slush. A
130 topographic shadow mask was applied to the data to avoid misclassifications. Furthermore, as lakes on the Greenland

Formatted: Strikethrough

Formatted: Strikethrough

Deleted: o

Deleted: advance, reduced

Formatted: Superscript

Deleted: missed, but

Ice sheet have been shown to form mainly within topographic sinks, only water areas within topographic depressions were retained using a Digital Elevation Model (DEM)-based sink mask, reducing the risk of identifying streams as lakes. Finally, a two-step cloud detection was applied, taking changes of lake area over time (step 1) and cloud (shadow) size into account. Depth and volume were not estimated, as no measurements of lake depths exist for similar latitudes (and thus solar zenith angles) within the observation period of Sentinel-2. Additionally, lakes on 79 °N Glacier have been shown to partially be significantly deeper than in West Greenland (see Neckel et al. (2020) and discussion section). As a consequence, spectrum-depth-equations derived in other studies could not be applied here.

Lakes are not automatically detected on the floating tongue portion of the glacier. Firstly, there are no topographic sinks, as these are reliant on a DEM of the grounded ice sheet. Secondly, the tongue is fast moving (approximately 1500 m a⁻¹; Krieger et al. 2020), which makes it difficult to track the lake outlines from one year to the next. Finally, melt water on the tongue is extensive and flows in more linear patterns as it drains through crevasses (Figure S1). Description of the SGLs on the floating tongue throughout the paper reflect only visual inspection of the satellite images.

2.2 In Situ Observations

Observational data at two AWSs located on Kronprins Christian Land (KPC) in the northeast of Greenland are used from the PROMICE (Programme for Monitoring of the Greenland Ice Sheet) network (<https://www.promice.dk>, last accessed 3 April 2019), operated by the Greenland and Denmark Geological Survey (GEUS). AWS KPC_U (Upper) is located at 79.83 °N, 25.17 °W, 870 m a.s.l and KPC_L (lower) is located at 79.91 °N, 24.08 °W, 370 m a.s.l (Figure 1). See Table 1 and Turton et al (2019) for more information on data availability and the climatology of this region.

Table 1: Location, elevation and data availability of KPC_L and KPC_U AWSs. Observations are taken approximately 2m about the surface. T is air temperature, SW_{in} and LW_{in} are the incoming (downward) short and longwave radiation respectively and TSK is the skin temperature of the glacier. See van As and Fausto (2011) for more information on observations from the PROMICE network.

Name	Location	Elevation (m a.s.l)	Data Availability	Variables used in this study
KPC_L	79.91 °N, 24.08 °W	380	01.01.2009- present	T, cloud cover; TSK SW _{in} , LW _{in}
KPC_U	79.83 °N, 25.17 °W	870	01.01.2009-14.01.2010, 18.07.2012-present	T, cloud cover; TSK SW _{in} , LW _{in}

2.3 Reanalysis data

The European Centre for Medium range Weather Forecasts (ECMWF) 5th generation reanalysis product ERA5 has been developed to replace the ERA-Interim product. ERA5 was gradually released starting in July 2017, and back to 1979 is now available. The horizontal resolution of ERA5 is approximately 31km and has 137 levels in the vertical from the surface to a height of 0.01hPa. Total precipitation and snowfall have been extracted from ERA5 at hourly intervals from the nearest grid point to the coordinates of the AWS. The ratio of snowfall to total precipitation (SF/TP) is then calculated. Total precipitation and snowfall estimates from ERA5 were compared to observations taken from buoy

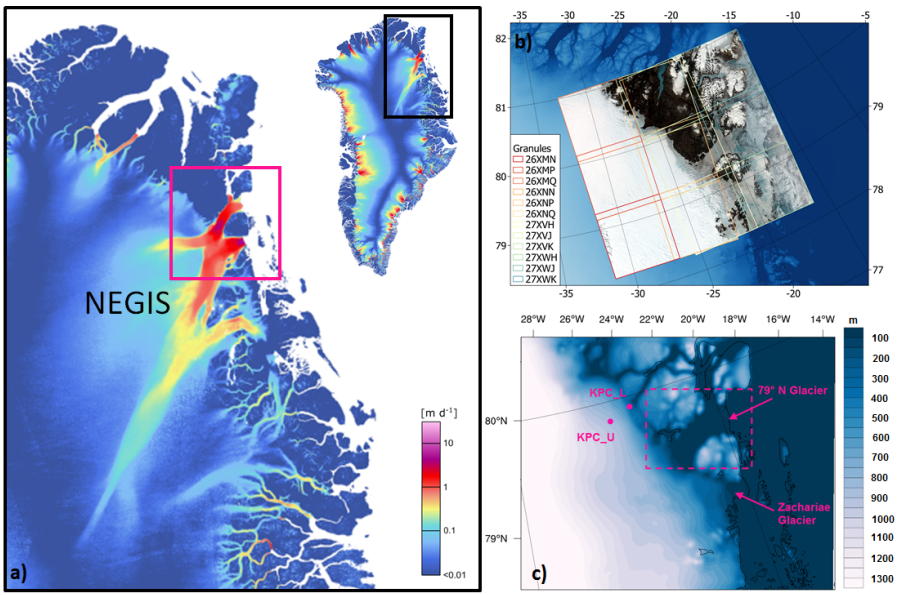
167 measurements in the Arctic Ocean by Wang et al (2019) and found to have a high degree of agreement with
 168 observations. The high resolution of ERA5 was also desirable compared to other available reanalysis products in the
 169 region (Turton et al. 2018).

170

171 **2.4 Polar Weather Research and Forecasting Model**

172 Archived model output from the Polar Weather Research and Forecast (PWRF) model (v3.9.1.1) is analysed.
 173 Meteorological variables are available at daily temporal and 1 km spatial resolution from Turton et al. (2019b) at
 174 <https://doi.org/10.17605/OSF.IO/53E6Z>. PWRF is a polar-optimised version of the WRF model, to better account for
 175 sea ice and snowpack processes (Hines et al 2015). The majority of adjustments in Polar WRF compared to regular
 176 WRF are located in the Noah land surface module. The model output has been previously evaluated against the in-situ
 177 PROMICE weather stations near 79 °N Glacier and can successfully represent a number of near-surface meteorological
 178 variables for both daily mean and sub-daily timescales (Turton et al. 2020). The full description and justification of the
 179 model setup is provided in Turton et al. (2020) and the inner domain location is presented in Figure 1a. Data are
 180 available from October 2013 to December 2018.

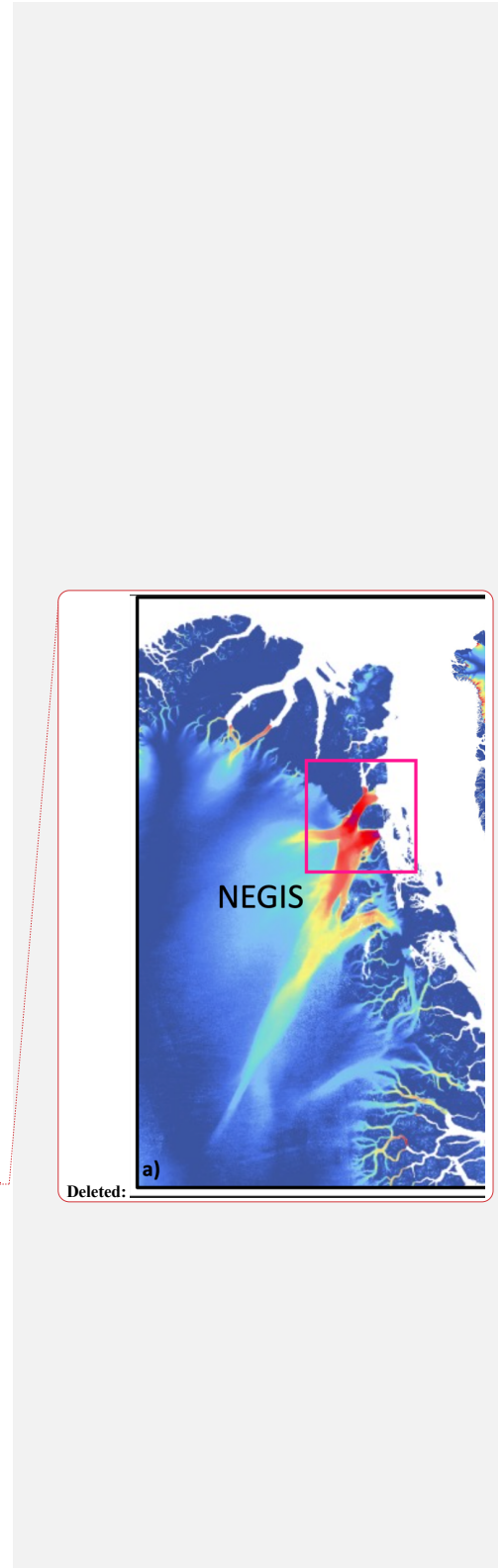
181



182

183 **Figure 1:** a) Ice velocity ($m d^{-1}$) of the northeast of Greenland with the North East Greenland Ice Stream (NEGIS) labelled
 184 (insert is the whole map of Greenland with ice velocities and a black box outlining the area in a). Pink box outlines the
 185 approximate area of b and c. b) The mosaic of Sentinel 2 granules used to apply the SGL detection algorithm, captured on
 186 June 19th, 2019. The background is GIMP DEM of Howat et al. (2014). c) The inner domain of Polar Weather Research and
 187 Forecasting (PWRF) model simulations by Turton et al. (2020), with the location of the two AWSs (KPC_U and KPC_L) and
 188 the elevation of the glacier and ice sheet in colour. The dashed pink box highlights the floating portion of the glacier. Ice
 189 velocity data from Sentinel 1, winter campaign from December 2019 to January 2021, from ESA Ice Sheets CCI project
 190 (<http://products.esa-icesheets-cci.org/products/downloadlist/IV/>; last accessed June 20th, 2021).

191



193 **2.5 COSIPY Mass balance model**

194 To provide an overview of the Surface Mass Balance (SMB) of the region, output from a distributed, open-source SMB
195 model called COSIPY (COupled Snowpack and Ice surface energy and mass balance model in PYthon)
196 (<https://github.com/cryotools/cosipy>; Sauter et al. 2020) is used. Hourly, 1 km spatial resolution surface mass balance
197 simulations from COSIPY, forced with 4d PWRP output for 2014 to 2018 are used here (COSIPY-WRF). COSIPY-
198 WRF SMB outputs were evaluated against available observations and compared to previous studies by Blau et al.
199 (2021) and found to represent the majority of SMB components with reasonable success at the grounding line and
200 inland for 79 °N Glacier. Archived output from COSIPY-WRF is available at: <https://doi.org/10.5281/zenodo.4434259>.
201 Here, we use surface mass balance estimates from September 2015 to August 2018 to place our melt pond findings into
202 context of the wider melt in the region. For a full list of parameterisations and description of COSIPY, see Blau et al.
203 (2021).

204

205 **3 Results**

206 **3.1 Interannual Characteristics**

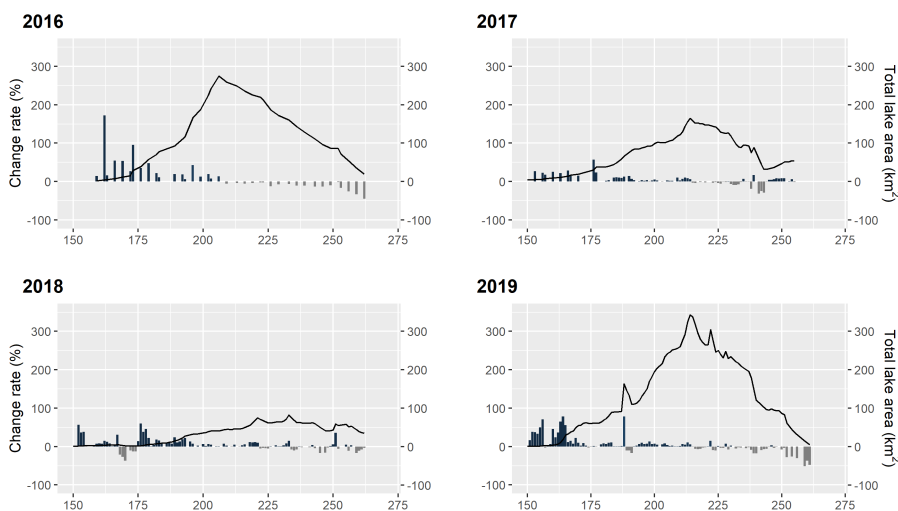
207 Here, we highlight the important lake characteristics and analyse the climatic and topographic controls responsible for
208 the spatial and temporal distribution of SGLs on 79 °N Glacier, as detected by Hochreuther et al. (2021) from 2016 to
209 2019. The average size of individual SGLs varies interannually from a maximum of 0.07 km² in 2016 to 0.02 km² in
210 2018.

211 Typically, lake development began in early June at the lowest elevations. Total lake area increased throughout
212 June and July, reaching a peak in the first week of August. Throughout July, the rate of increase was steady, with
213 approximately 20-25 % increase in lake area from one observation to the next, in all years (Figure 2). From mid-August
214 (day 220-230), the daily change rate became negative as SGLs freeze up or drain. However, in some years there were
215 still individual days of increasing SGL area (positive change rate) punctuating the overall decline in SGL area towards
216 the end of the melt season (Figure 2). This occurred due to periods of warm air temperature or late-season rainfall
217 events. SGLs which remained at the end of the melt season (and have not drained into the firm or channels), typically
218 froze over or became buried in snow. Freeze over of lakes started with a growing floe on one side or with a ‘lid’ in the
219 centre and freezes outwards (Figure 3). In years with low snow accumulation at the start of September, the frozen, semi-
220 spherical remains of frozen lakes can still be seen.

221 The rate of increase in SGL area varied interannually (Figure 2). The years 2016 and 2019 were characterised
222 by fast increases in SGL area in June (days 150 to 170-180). In 2016, the increasing rate of SGL area regularly
223 exceeded 100% increase in total SGL area from one observation to the next (Figure 2). June 2017 had a relatively
224 steady increase in SGL area, with approximately 25 % daily increases in area. June 2018 was characterised by a see-saw
225 pattern in expansion of lake area, with periods of fast increases in area (approximately 50% daily increases), followed
226 by periods of SGL lake closure (Figure 2). Sustained expansion of lake area only occurred after the last week of June
227 for 2018. Closure or freeze-over of lakes at the end of the melt season was later and slower in 2018 than in 2016, 2017
228 and 2019 (Figure 2), and some lakes even remained open at the end of the observation period in mid-September.

229

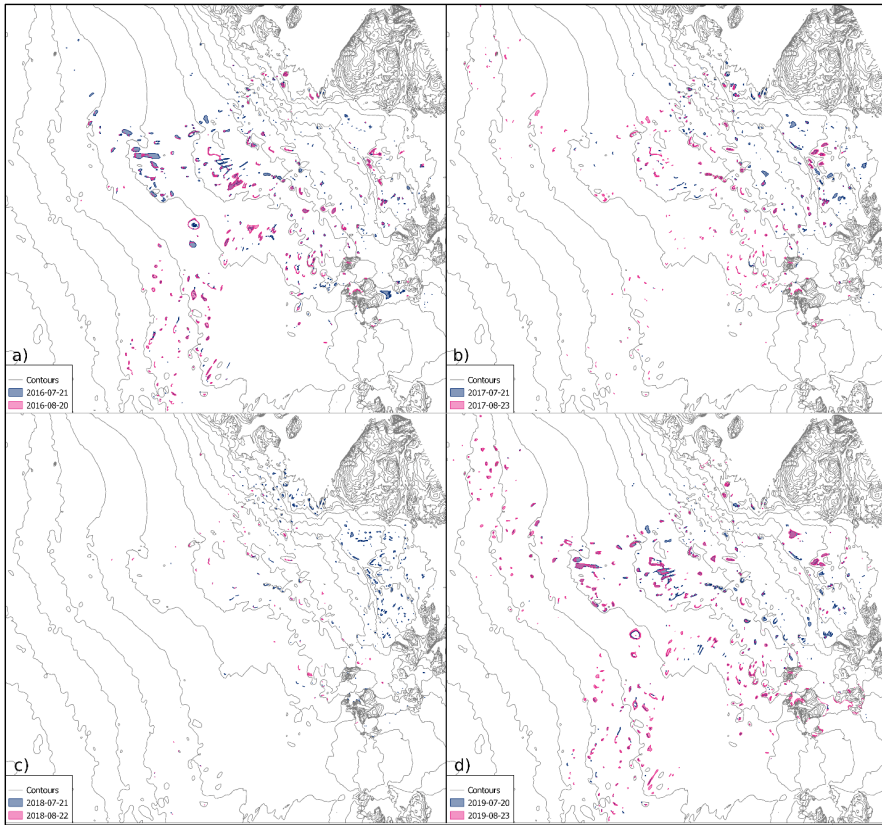
230



231
 232 **Figure 2: Change rates of the lake area between observations from 2016 to 2019, limited to DOY 150 – 270 (bars, in percent**
 233 **of the last observed area). Line graph: Total lake area in km².**
 234

235 Similar to the rate of change, the total SGL area varied interannually. The largest peak total SGL area was seen
 236 in 2019, with 330 km² (Figure 2). Conversely, the smallest peak total SGL area was in 2018 with just 77 km²
 237 (Hochreuther et al. 2020). This is approximately a 329 % increase between maximum lake area in 2018 and in 2019.
 238 The spatial difference in the years is shown in Figure 3, where considerably more lakes are highlighted in 2016 and
 239 2019 than in either 2017 or 2018. Whilst this only shows a snapshot of conditions on two different days, representing
 240 peak conditions (mid-July; blue) and a period when the SGLs freeze up (mid-August; pink), the spatial distribution of
 241 the lakes differs by years. SGLs at elevations greater than 800m are detected across much of the glacier in 2016 and
 242 2019, but only sparsely in 2017 and 2018 (Figure 3 and 4). Similarly, much larger SGLs are open in 2016 and 2019 than
 243 the other two years (Figure 3). The peak total SGL area in 2016 and 2019 was considerably larger than in 2017 and
 244 2018, especially at altitudes from 1000 to 1600 m a.s.l (Figure 4). However, in years with a lower total SGL area, such
 245 as 2018, the distribution of lakes is skewed more towards lower elevations (Figure 4c).

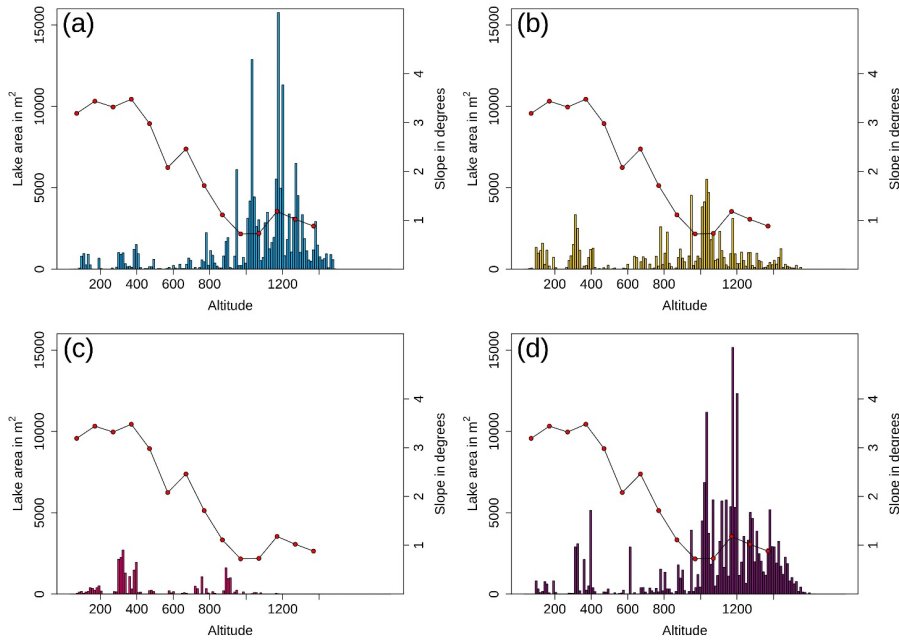
246
 247
 248
 249
 250



251
 252 **Figure 3: Lake area in July (blue) and August (purple) for 2016 (a), 2017 (b), 2018 (c) and 2019 (d). Contours are every 100m.**
 253 **Lakes on the tongue have been removed to assess only those controlled by topography.**
 254

255 **3.2 Topographic Controls**

256 Melt lakes are part of the whole drainage system of ice sheet hydrology. Given sufficient meltwater
 257 availability, the location of lake formation is foremostly controlled by the topography of the ice sheet surface (Lüthje et
 258 al 2006). Lakes therefore act as a sink for the englacial channels which distribute the water across and through the ice
 259 sheet. The position of lakes on the Greenland Ice Sheet is therefore largely controlled by the underlying bedrock
 260 topography (Lampkin and Vanderberg, 2011).



261
 262 **Figure 4: Altitude distribution of lake area for the maxima of 2016 (a), 2017 (b), 2018 (c) and 2019 (d) per 10m altitude**
 263 **difference. Red dots show average slope angle for 100m altitude bins.**

264
 265 Below the grounding line of 79 °N Glacier (on the floating tongue), the lakes advect downstream with the flow of the
 266 glacier towards the ocean, in a similar fashion to those observed on Petermann Glacier (Macdonald et al. 2018).
 267 However, above the grounding line, lakes develop in the same depression or location each year (Figure 3). The SGL
 268 area in 2016 and 2019 is larger compared to 2017 and 2018. This interannual change in SGL area is due to the inland
 269 expansion of lakes to higher elevations (Figure 3), as opposed to the development of new lakes at lower elevations.

270 The minimal SGL area between approximately 200 m and 600 m (Figure 4) is partly a consequence of higher
 271 slope angle. The slope of the glacier surface between these altitudes is approximately 3 ° to 4 °. The areas with larger
 272 SGL area and where the largest lakes develop (Figure 3) is between 0.6 ° and 1.5 ° (Figure 4). Unlike some of the ice
 273 shelves in Antarctica, where SGLs are concentrated around the grounding line due to low elevation and slope (Arthur et
 274 al. 2020), on 79 °N Glacier, SGLs are also clustered at higher altitudes, where low slope angles are also measured.
 275 Consequently, the largest lakes can be found at altitudes between 850m and 1000m. The highest elevation of SGL
 276 development was at 1600 m in 2019 (Figure 4). Due to the flat terrain, these lakes are, judging from the blue spectrum
 277 saturation, comparatively shallow, whereas the lakes close to the grounding line appear smaller in area but deeper
 278 (Figure S2).

279 Significant decreases of total lake area can be attributed either to sudden climatic changes, or to consecutive
 280 drainage events. In 2019, the sudden decrease around DOY 240 is attributed to a large freeze-over of the majority of all
 281 lakes above 700 m a.s.l. Conversely, the decrease following the 2019 peak of total lake area on August 2nd (DOY 214)
 282 was caused by a step-wise drainage pattern, starting with larger lakes at high altitudes, followed by drainage events
 283 close to the ice front of Zachariae and accompanied by a speedup of calving and seawater movement (Figure S3).

284 Because of the timing and sequence of the rapid drainage events, we can deduce a subglacial meltwater reconfiguration
285 in this case.

286

287 3.3 Climatic Controls

288 Whilst the location of the individual lake is controlled by topographic features, whether or not the lake will develop is
289 due to atmospheric conditions. In conjunction with the topographic controls, the second most important control for lake
290 development is the availability of melt water, which is largely controlled by the weather conditions. We have assessed
291 numerous atmospheric variables for the four-year period, in an attempt to investigate the relationship between these
292 variables and the melt onset and extent.

293 Buzzard et al. (2018a) investigated the impact of varying atmospheric variables in an idealised 1-D melt pond
294 model and identified that near-surface air temperature (T_a), skin (or surface) temperature (TSK), shortwave incoming
295 radiation (SWin) and snowfall (SF) had a considerable impact on the development of SGLs. We investigate these
296 variables in conjunction with rainfall following the findings of Oltmanns et al. (2019). Other previously investigated
297 variables which had little to no influence on SGL development include wind speed and non-climatic variables such as
298 wet-snow albedo (Buzzard et al. 2018a), which we do not investigate.

299

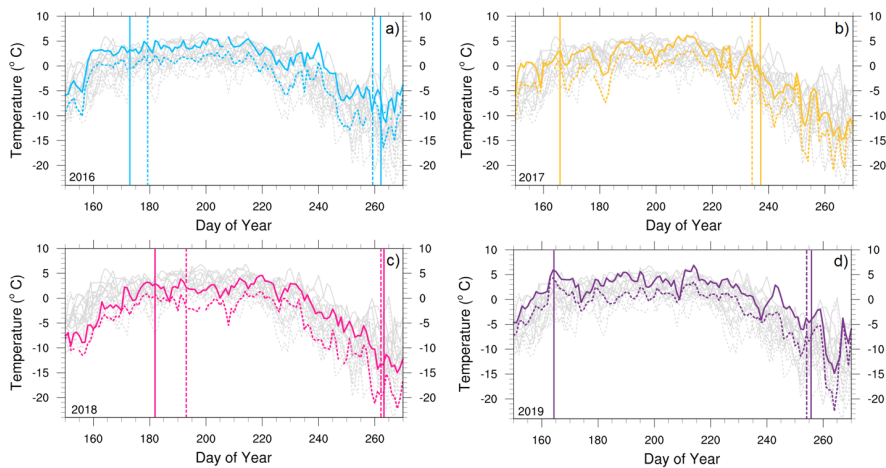
300 3.3.1 Air Temperature (T_a)

301 The average summer (JJA) T_a is $0.7\text{ }^{\circ}\text{C}$ over the floating tongue of the glacier, decreasing to $-1.2\text{ }^{\circ}\text{C}$ at an elevation of
302 830 m a.s.l observed at KPC_U AWS (Turton et al 2019). The average June, July and August air temperatures at
303 KPC_L (KPC_U) are $1.1\text{ }^{\circ}\text{C}$ ($-2.1\text{ }^{\circ}\text{C}$), $3.6\text{ }^{\circ}\text{C}$ ($0.7\text{ }^{\circ}\text{C}$) and $0.5\text{ }^{\circ}\text{C}$ ($-2.6\text{ }^{\circ}\text{C}$) respectively (see Figure 1 for AWS
304 locations). Typically (from 2009-2019), the daily average T_a reaches $0\text{ }^{\circ}\text{C}$ in the second week of June at approximately
305 390 m a.s.l (KPC_L location), and late June at 830 m a.s.l (at KPC_U location) (Table 2). From this date until mid-
306 August, the daily air temperatures are often at or just above the melting point (Figure 5).

307 In 2016, all three summer months observed above average T_a at both observation sites. At higher elevations,
308 daily T_a reached $0\text{ }^{\circ}\text{C}$ slightly earlier than usual (June 11, 2016), after a cooler than average start to June, especially at
309 KPC_U (Figure 5a). Rather than a gradual increase in air temperatures throughout the start of June, there was a marked
310 jump in temperature between June 5 and June 11, 2016 (Figure 5a). At KPC_U the temperature increased from $-10.1\text{ }^{\circ}\text{C}$
311 on June 5 to $0.9\text{ }^{\circ}\text{C}$ on June 11, and then remained above or close to freezing ($0\text{ }^{\circ}\text{C} \pm 0.75\text{ }^{\circ}\text{C}$) until mid-August
312 (Figure 5a). Just 16 days after this temperature jump, SGL formed at elevations of approximately 870 m a.s.l (elevation
313 of KPC_U) (Table 2; Figure 5a). There were 84 days (70 of which were consecutive) with above-zero daily T_a in 2016
314 at KPC_L (Table 2). The longest consecutive period with above average air temperatures at both KPC_L and KPC_U,
315 from observations between 2009 and 2019, was during 2016. The average June 2016 T_a , simulated by PWRF, was
316 above freezing for large parts of the NEGIS region (Figure 6a). Spatially, these higher air temperatures approximately
317 follow the 800 m contour line, showing some agreement with the altitude-temperature relationship. However, the July
318 2016 average air temperatures deviate from this relationship, with warmer air temperatures above 1200 m for the $79\text{ }^{\circ}\text{N}$
319 Glacier but remaining below 800 m near Zachariae and to the south of the glacier (Figure 7a). Average July 2016 T_a
320 above $3\text{ }^{\circ}\text{C}$ is simulated for large parts of NEGIS. At KPC_L, July 2016 was $3.2\text{ }^{\circ}\text{C}$ warmer than average, agreeing well
321 with the PWRF data.

322 The earliest observation of above-zero daily T_a (from 2009 to 2019) was May 27, 2017 at KPC_L. However,
323 air temperatures rapidly decreased again at the end of May, 2017, before reaching $0\text{ }^{\circ}\text{C}$ on June 1, 2017 (Figure 5b).
324 Both June and August 2017 average air temperatures at both observation sites were slightly below average, but the July
325 average temperature was $0.5\text{ }^{\circ}\text{C}$ ($0.2\text{ }^{\circ}\text{C}$) warmer than the 2009-2019 average at KPC_L (KPC_U). Despite the lower

326 June Ta in 2017 compared to 2016, the length of time between Ta reaching above 0 °C at KPC_L and development of
 327 melt ponds at 370 m a.s.l. was also 14 days (Table 2; Figure 5b). However, at higher altitudes, there were only 5 days
 328 between Ta above 0 °C and melt ponds developing at 870 m a.s.l. in 2017 (Table 2; Figure 5b). The cooler air
 329 temperature in 2017 relative to the previous summer is evident over the majority of NEGIS, with above average Ta
 330 locations restricted to low elevation pockets (Figure 6b). The average 2017 Ta is spatially more similar to the 2016
 331 situation in July (Figure 7). In July 2017, Ta greater than 0 °C was simulated over much of the 79 °N Glacier, up to
 332 elevations greater than 1000 m a.s.l. Lower elevation regions, and areas of seasonally exposed rocks reached daily
 333 average Ta of 3 °C (Figure 7b). At higher elevations, the earliest closure of SGLs within the four-year period was
 334 observed in this year (September 1, 2017 at 870 m a.s.l), which was approximately 10 days after the Ta dropped below
 335 freezing at KCP_U (Figure 5b). Similarly, at lower elevations, 2017 saw the earliest SGL closure of the four-year
 336 period on September 12, 18 days after Ta dropped below freezing at KPC_L (Table 2; Figure 5b).
 337
 338



339 **Figure 5: The daily air temperature observations from KPC_L (solid line) and KPC_U (dashed line) from day of the year 150**
 340 **to 270 for a) 2016, b) 2017, c) 2018 and d) 2019. Grey lines are daily air temperature from 2009-2019 (when available).**
 341 **Vertical solid (dashed) lines represent the opening and closing of SGLs at KPC_L (KPC_U) approximate elevations**
 342 **(information from Table 2).**
 343
 344

345 The smallest total SGL area and latest lake development were observed in 2018. The latest observed onset of
 346 warm air temperatures was also in 2018, when the first recorded above-zero daily Ta was on June 20, 2018 (Figure 5c;
 347 Table 2). This is also evident in the later onset of SGLs at both lower and higher elevations (Figure 5c; Table 2). The
 348 first two weeks of June 2018 were colder than in any other year in the last decade of observations (Figure 5c). This is
 349 also reflected in the much colder June average Ta over the NEGIS region from the PWRP 2018 simulations (Figure 6c).
 350 All three summer months in 2018 were characterised by considerably cooler air temperatures over the area of interest,
 351 with above freezing temperatures restricted to very low-lying parts of the glacier during July (Figure 7). June and July
 352 2018 were both 2.0 °C cooler than average at both observation locations. Both the number of days above freezing and
 353 the consecutive number of days above freezing were both at their lowest in 2018 (Table 2), with just 8 consecutive days

354 above freezing at KPC_U. In August 2018, Ta increased and were close to average conditions throughout August
355 (Figure 5c). The last day with Ta above freezing was observed on August 25, 2018 at KPC_L, the same as in 2017
356 (Table 2). However, the latest observation of SGLs at 370 m a.s.l was September 18, 2018, the latest in the four-year
357 period, and SGLs were still visible at the end of the observational period (Table 2; Figure 5c).

358 At lower elevations, the conditions in summer 2019 were remarkable. At both KPC_L and KPC_U, air
359 temperature records were broken in June 2019 (Figure 5d), along with most areas of the ice sheet (Tedesco and
360 Fettweis, 2020). There were 115 days of Ta greater than 0 °C with 61 of those being consecutively observed at KPC_L
361 in 2019 (Table 2). Similarly, warm Ta continued past the summer season, with the final observation of Ta above 0 °C
362 on September 28, 2019 (Table 2). On June 12, 2019, a new daily air temperature record was set at KPC_U of 4.2 °C,
363 swiftly broken by a new daily record on June 13 of 4.3 °C. Prior to these two days, the highest temperature had been
364 during the record-breaking summer of July 2012. Similarly, an hourly maximum of 7.9 °C was recorded at KPC_U,
365 which is the highest hourly temperature observation in a decade. Despite a warm start to the season, air temperatures
366 returned to normal for the remainder of June and July. A second peak temperature event was recorded in early August
367 2019. The highest daily air temperature record at KPC_L (between 2009 and 2019) of 6.9 °C was observed on August
368 2, 2019. The spatial distribution of the Ta in summer 2019 is not analysed as PWRP simulations are not available for
369 this period. However, satellite images reveal extensive surface melt pond formation, very thin and broken sea ice, and a
370 50 km² calving event of Spalte Glacier was also recorded this year (Figure S1). When taken altogether, these
371 characteristics point to particularly warm temperatures across the whole region in 2019. SGL development started
372 earlier in 2019 than in 2016 despite both years observing Ta above 0°C at a similar time (June 6 in 2019 and June 7 in
373 2016) (Table 2; Figure 5a,d).

374

375 3.3.2 Skin Temperature (TSK)

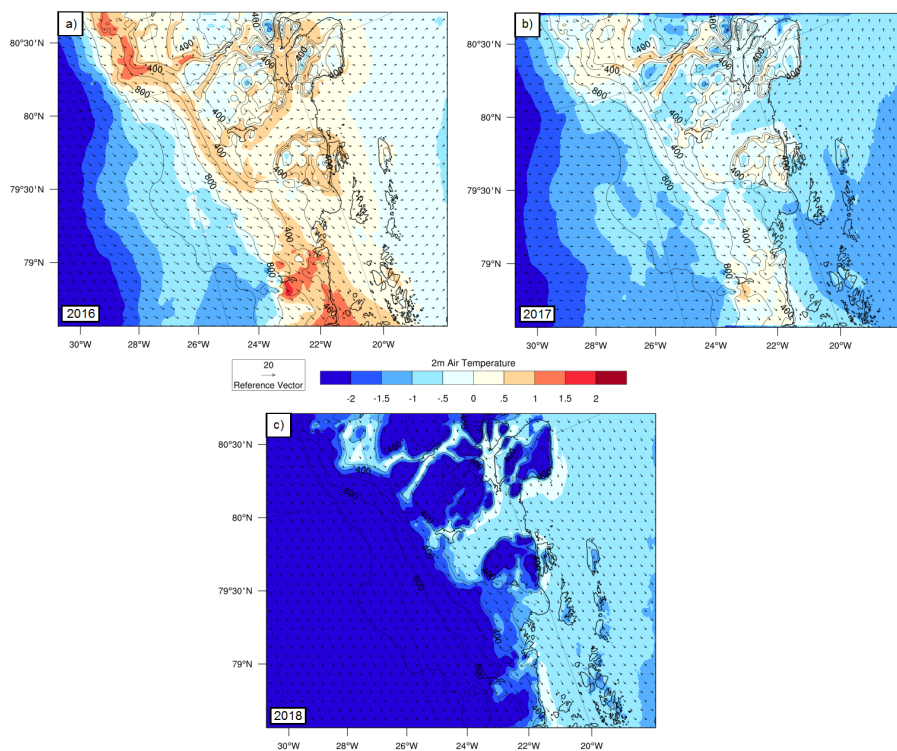
376 When daily average TSK is at 0 °C, the term TSK_{melt} is used in this manuscript to represent likely surface
377 melting. At KPC_L, the average (2009-2019) melt day onset is June 18, whereas at KPC_U this date is June 28. The
378 average number of days with TSK_{melt} is 44 at KPC_L and 12 at KPC_U. The average number of consecutive TSK_{melt}
379 days is 21 at KPC_L and 5 at KPC_U.

380 In terms of the skin temperature of the glacier at KPC_L location, 2016 stands out. The largest number of
381 TSK_{melt} days and longest number of consecutive TSK_{melt} days were observed in 2016 (64 days, of which 47 were
382 consecutive). Similarly, the earliest onset of TSK_{melt} in the four-year period was observed at KPC_L in 2016, on June 9.
383 At KPC_U, the number of TSK_{melt} days and consecutive TSK_{melt} days were also above average for 2016, however the
384 onset of surface melt was later than usual (July 1). Not only was this a stand-out year at KPC_L from the four-year
385 study period, but also in the observational record from 2009. Even the record-breaking melt year of 2012 had fewer
386 TSK_{melt} days and consecutive melt days.

387 The year 2017 was a relatively average melt season in terms of TSK_{melt}. The onset of TSK_{melt} at KPC_L was on
388 June 13 (only 5 days earlier than average) and there were 46 TSK_{melt} days, of which, 17 were consecutive. At KPC_U,
389 the melt onset was earlier than average (June 10) but the number of TSK_{melt} days and consecutive melt days were lower
390 than average (9 and 3 days respectively). The latest melt onset date was observed in 2018 at both locations; June 26 at
391 KPC_L (8 days later than average) and August 3 at KPC_U (36 days later than average). At KPC_U, only one day
392 observed TSK_{melt} and only 30 days (13 consecutive) experienced TSK_{melt} at KPC_L. Therefore, the shortest melt
393 duration and latest melt onset at both locations were observed in 2018.

394 The year 2019 has a distinct spatial characteristic in terms of TSK_{melt}. At lower elevations, the number of
395 TSK_{melt} and consecutive TSK_{melt} days are below average (27 and 17 respectively). However, at higher elevations,

396 melting is above average with 17 TSK_{melt} days, of which 6 were consecutive. At KPC_U, TSK_{melt} onset was also earlier
 397 than average. Despite the above average Ta at PKC_L and KPC_U in 2019, only above average TSK conditions were
 398 observed at KPC_U.
 399



400
 401 **Figure 6: The monthly average 2m air temperature from PWRF runs for June 2016 (a), 2017 (b) and 2018 (c). Simulations**
 402 **were not available for 2019. Contours are every 200 m, with labels every 400 m. Black arrows are wind vectors displaying**
 403 **monthly average wind direction and speed, with a reference vector of 20 ms⁻¹ provided.**
 404

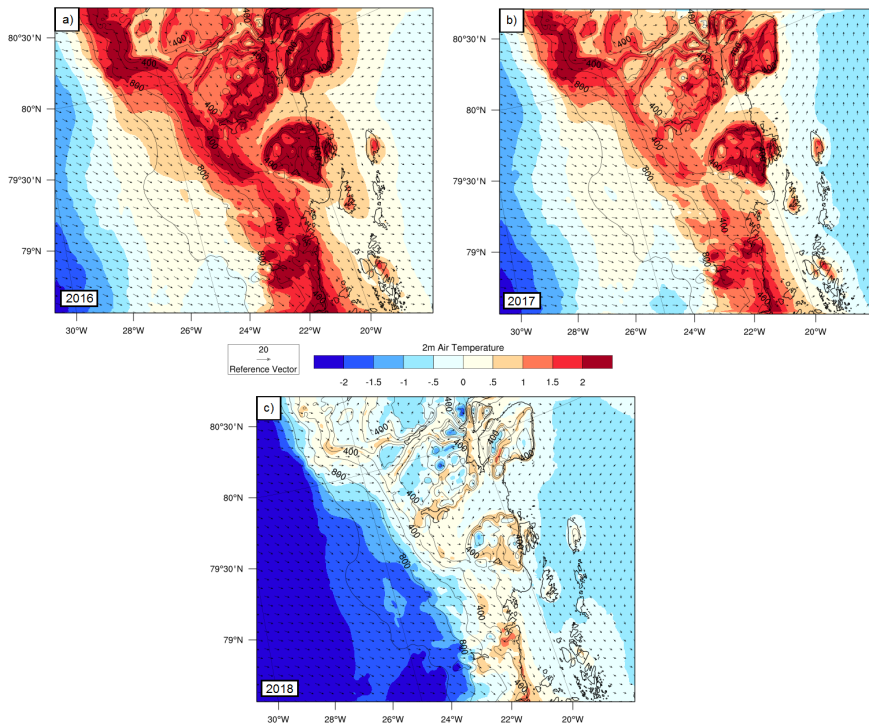
405 3.3.3 Incoming Shortwave Radiation (SWin)

406 In 2016, June and July both experienced positive biases in SWin at both observation sites. At KPC_L, the SWin was 7.3
 407 Wm^{-2} and 16.7 Wm^{-2} higher than average for June and July (respectively). At KPC_U, a positive bias of 10.2 Wm^{-2}
 408 during June and 6.4 Wm^{-2} in July was observed in 2016. There was also a positive bias of 17.3 Wm^{-2} and 7.5 Wm^{-2}
 409 observed in July 2017 (KPC_L and KPC_U respectively). This increase in SWin observed at the surface is attributed to
 410 less cloud cover in the region. Cloud cover (fraction) at the KPC stations is estimated from downwelling longwave
 411 radiation and air temperature (both of which are observed) (Van as 2011). There was a reduction in cloud cover fraction
 412 in June, July and August in 2016 at both locations. The average summer cloud cover fraction at both locations is 0.4,
 413 whereas in 2016 it was 0.3. The reduced cloud cover is further evident in the sentinel images, with many more clear-sky
 414 days over NEGIS in 2016 than 2017 or 2018.

415 The SWin was lower than average at both observation sites in June 2017 (-2.6 Wm² at KPC_U and -10.5 Wm²
416 ² at KPC_L). There was a positive bias in SWin of 17.3 Wm² and 7.5 Wm² observed in July 2017 (KPC_L and
417 KPC_U respectively), revealing clear skies in July. At lower elevations, this positive bias continued into August, with a
418 monthly average bias of 6.7 Wm² at KPC_L. However, at KPC_U, a negative bias of -8.5 Wm² was observed.

419 Despite the cooler conditions at both locations in summer 2018, positive biases in SWin were observed at both
420 locations in July and August. The July SWin average was 32.7 Wm² and 18.4 Wm² higher than the 2009-2019 average
421 at KPC_L and KPC_U, respectively. Similarly, the August SWin positive bias was 18.9 Wm² at KPC_L and 17.3 Wm²
422 at KPC_U. Higher than average cloud cover in June (0.45 compared to 0.36 at KPC_U) and lower than average in July
423 and August provide further evidence for clearer skies in the mid to late summer. The positive SWin and average
424 temperatures towards the end of summer 2018, together with a considerable amount of liquid water from the melted
425 snowpack, likely provided optimal conditions for the later peak in maximum SGL area and slower freeze over of the
426 lakes, with many still remaining open at the end of the observational period in September 2018 (Table 2).

427 Some of the largest anomalies of SWin were observed in summer 2019, with KPC_L and KPC_U observing
428 monthly negative anomalies of -30.0 Wm² and -19 Wm² respectively, for June, despite the high temperatures.
429 Conversely, July saw opposite anomalies, with large positive anomalies in SWin at both KPC_L (+35.4 Wm²) and
430 KPC_U (+34.3 Wm²). Similarly, the July average cloud cover was considerably below average, with a value of 0.24
431 compared to an average of 0.36 at KPC_U. A persistent high-pressure system was responsible for the early-season
432 temperature and melt increases seen over the whole ice sheet (Tedesco and Fettweis, 2020). However, increased
433 cloudiness observed in the northeast of the ice sheet (and also simulated by Tedesco and Fettweis, 2020) also
434 contributed to the early melt onset in June.



435
 436 **Figure 7: The monthly average 2m air temperature from PWRP runs for July 2016 (a), 2017 (b) and 2018 (c). Simulations**
 437 **were not available for 2019. Contours are every 200 m, with labels every 400 m. Black arrows are wind vectors, displaying**
 438 **monthly average wind direction and speed, with a reference vector of 20 ms⁻¹ provided.**
 439

440
 441 **Table 2: The timing of the first (last) daily average Ta greater than 0 °C (Ta > 0 °C), number of days with daily Ta greater**
 442 **than 0 °C and earliest development (freeze up) of melt ponds at elevations closest to the AWS elevations. 370 m a.s.l. relates to**
 443 **KPC_L elevation and 870 m a.s.l. relates to KPC_U elevation. *One day observed just below 0 °C in this period. ** end of**
 444 **sensing period. Melt pond development and freeze over dates are represented in Figure 5.**

Year	AWS	Ta > 0 °C	# days Ta > 0 °C (consecutive)	SGL develop at 370 m/870 m elevation	Ta consistently < 0 °C	SGL freeze over at 370 m/870 m elevation
2016	KPC_L	June 7	84 (70*)	June 21	Aug 30	Sep 18**
	KPC_U	June 11	79 (44)	June 27	Aug 29	Sep 15
2017	KPC_L	June 1	85 (39)	June 15	Aug 25	Sep 12

	KPC_U	June 10	73 (16)	June 15	Aug 22	Sep 1
2018	KPC_L	June 20	66 (38)	July 1	Aug 25	Sep 20**
	KPC_U	June 26	51 (8)	July 12	Aug 16	Sep 19
2019	KPC_L	June 6	115 (61)	June 13	Sept 29	Sep 13
	KPC_U	June 12	67 (14)	June 13	Aug 18	Sep 11

445

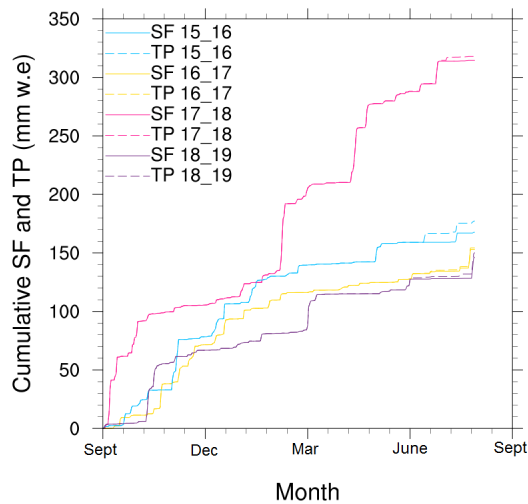
446 3.3.4 Total Precipitation (TP) and Snowfall (SF)

447 As precipitation is not observed at the KPC stations, we have used ERA5 data. Following Wang et al (2019), a
448 high ratio of snowfall to total precipitation can be inferred as more snow, whereas a low ratio means more precipitation
449 fell as rain than snow. Between September 2015 and May 2016 (accumulation period), 160mm of cumulative snowfall
450 fell at the KPC_U location. The ratio of snowfall to total precipitation was 1.0, meaning that all precipitation fell as
451 snow. However, during summer 2016, especially July and August, some rainfall is present in the region (Figure 8). In
452 July 2016, all 7.7 mm of cumulated precipitation was liquid rain (ratio of 0), and in August, the ratio was 0.82 with 1.9
453 mm of rainfall. For the whole summer period (JJA), the ratio was 0.5. Even though the summer was therefore relatively
454 dry, there was still a larger amount of summer rainfall in 2016 than in other years.

455 Total accumulated snowfall between September 2016 and May 2017 at KPC_U was approximately 130 mm
456 w.e, which is the second lowest total amount in our four-year period of interest (Figure 8). The summer (JJA) 2017
457 snowfall to total precipitation ratio was 0.96, highlighting the minimal rainfall in this year: the smallest rainfall total in
458 the four-year period.

459 The largest amount of cumulated snowfall during the accumulation period (September to May) occurred in
460 2018 with 277.9 mm (Figure 8). In the other years of interest, the cumulated snowfall total was less than 190 mm. There
461 were a number of large snowfall events in 2018 which contributed to the larger total precipitation. For example,
462 between February 22 and February 26, 2018, 56.5 mm w.e snowfall fell in the region, which is more than the winter
463 (DJF) total snowfall in 2015/2016. The regular fresh snow episodes increased the albedo and reflected shortwave
464 incoming radiation at the start of the summer season. A thick, fresh snowpack also has a low density, with more space
465 for liquid water to penetrate instead of sitting on the surface in SGLs. The switch from SGL area increase (lake
466 development) to decrease (freeze up) and back again during June 2018 (Figure 2) was due to a number of snowfall
467 events in June, which covered any exposed SGLs. The continuous input of snowfall throughout the year and into
468 summer delayed the onset of SGL development at 870 m a.s.l to mid-July 2018 (Table 2), which was the latest in the
469 four-year period.

470



471
472 **Figure 8: The cumulative total precipitation (TP) and snowfall (SF) from September (beginning of the accumulation season)**
473 **to August (end of melt season) at KPC_L location from ERA5.**
474

475 The smallest accumulated snowfall from 2016 to 2019 occurred in 2019, with only 125 mm falling by May
476 2019 (Figure 7). The particularly shallow snowpack provides less water storage availability and lower albedo values,
477 which likely led to the earlier SGL detection in 2019 compared to the other warmer than average year of 2016. The later
478 refreeze of SGLs in the previous summer may also have contributed to the earlier detection in 2019. At the end of
479 August 2019, 21 mm of snowfall occurred, which started the new accumulation season earlier than in previous years
480 (Figure 8). Visual analysis of Sentinel 2 data reveals that between August 30 and September 16th, 2019 there were very
481 few melt ponds detected due to thick cloud cover. On September 20, 2019, there is evidence of fresh snowfall and very
482 few pond outlines remaining, which agrees with the ERA5 analysis of snowfall towards the end of August and start of
483 September.
484

485 **3.3.5 Climate Influence Summary**

486 Summer 2016 experienced the largest average individual SGL size (0.07 km²), second largest total SGL area
487 and second fastest rate of SGL area growth in our four-year record. A combination of above average air temperatures,
488 particularly in mid-June and July, and a large amount of liquid precipitation during summer was likely responsible for
489 the rapid SGL development and peak in total SGL area in late July. Despite the early observation of Ta above freezing
490 in 2017, the earliest in our four-year period, the June 2017 average Ta was slightly below average. This, combined with
491 the slightly above average July 2017 temperatures, likely led to the slower rate of increase in SGL area in 2017
492 compared to 2016 (Figure 2), and peak in maximum area in early August 2017. The thinner snowpack and limited
493 amount of liquid precipitation falling during summer contributed to the lower maximum SGL area of 153.26 km² in
494 2017, compared to 265.39 km² in 2016. In 2018, the spatial distribution of SGLs was different to the other three years,
495 with the largest SGL area at elevations between 300 m and 400 m a.s.l (Figure 4). Very few SGLs were observed at
496 elevations greater than 900 m, leading to smaller average individual SGL area, as no larger lakes at higher elevations

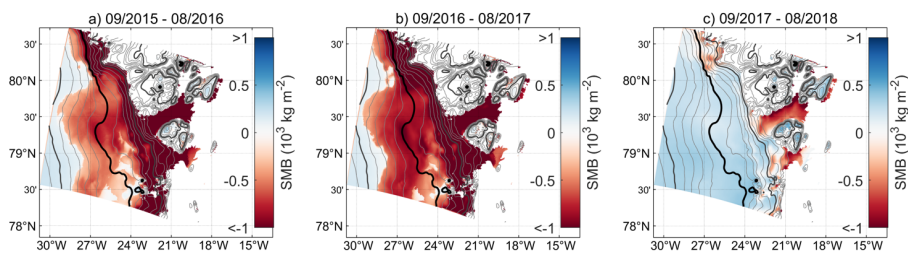
Formatted: Font colour: Red, Strikethrough

Formatted: Indent: First line: 1.25 cm

497 were identified (Figure 3). Average individual lake size in 2018 was 0.02 km^2 , compared to 0.07 km^2 in 2016, 0.06 km^2
 498 in 2017 and 2019. A combination of the cooler air temperatures at the start of summer (see Section 3.3.1) and thick
 499 snowpack led to the delayed onset of SGL development, lower maximum altitude of SGLs and lower total SGL area in
 500 2018 (Figure 3). Total SGL area was largest in 2019, even though the average size of individual SGLs was the same as
 501 in 2017 (0.06 km^2). A combination of higher air temperatures, more days above freezing and a smaller snowpack at the
 502 start of the melt season all contributed to a significantly higher total SGL area in 2019 (Figure 4). The peak melt pond
 503 area at the start of August 2019 coincides with an air temperature peak of $6.9 \text{ }^\circ\text{C}$ on August 2nd at KPC_L, the warmest
 504 daily T_a ever recorded here (Figure 5).

505 To summarise the climatic conditions: We find that a combination of above average air temperatures, a thin
 506 pre-summer snowpack and summer precipitation falling as rain during summer 2016 and 2019 led to the exposure of a
 507 large number of SGL over a much larger area than observed in the two other years. Conversely, a large amount of
 508 snowfall preceding the melt season and below average air temperatures in 2018 led to the development of very few
 509 SGLs, which were restricted to the lower elevation areas.

510



511
 512 **Figure 9: The annual surface mass balance of the 79°N glacier and NEGIS region from September to the following August in**
 513 **2015-2016 (a), 2016-2017 (b), 2017-2018 (c). There are no estimates for 2018-2019 as the PWRP simulation which is used as**
 514 **input to the COSIPY SMB model was only available until December 2018. The dark black contour marks 1000m a.s.l and the**
 515 **grey contours are every 100m.**
 516

517 3.4 Surface mass balance

518 To assess whether high areas of SGL development relate to the Surface Mass Balance (SMB), the COSIPY
 519 SMB estimates from Blau et al. (2021) are used. COSIPY has been previously tested for a number of glaciers in Tibet
 520 (Sauter et al. 2020) and evaluated for 79 °N Glacier by Blau et al. (2021). The SMB estimates from September to the
 521 following August for 2015 to 2018 are shown in Figure 9 (2018 to 2019 was not simulated, as COSIPY uses the PWRP
 522 output as atmospheric input). Spatially, the SMB is similar in 2015/2016 to 2016/2017, despite the warmer summer of
 523 2016. Low-lying areas of the 79 °N Glacier tongue, Zachariae Glacier and areas up to 1000 m a.s.l. were in a negative
 524 SMB area in 2015/2016. The following year, the negative SMB extends further inland and to higher altitudes up to
 525 1300m a.s.l (Figure 9). The similarity in SMB between 2015/2016 and 2016/2017 is further presented in Figure 10.
 526 Vertically, the annual SMB profiles are similar in 2015/2016 and 2016/2017 with a negative SMB up to 1400 m a.s.l
 527 (Figure 10a). The summer SMB remains negative up to elevations of 1600 m a.s.l. for both 2016 and 2017, which
 528 coincides with the approximate maximum elevations of SGLs in these years (Figure 4a, b). The annual and summer
 529 SMB in 2018 is considerably different to the previous two years. The annual SMB is negative only at elevations less
 530 than 400 m (Figure 10), which is restricted to areas of the floating tongue only (Figure 9). The summer SMB is also
 531 only negative up to 1000 m a.s.l. which also pinpoints the maximum elevation of SGLs in 2018 (Figure 4c).

Formatted: Font colour: Red

532 It is likely that expansion of melt ponds at higher elevations is partly controlled by spikes in the SMB
533 immediately prior to pond development, especially towards the end of the melt season. In summer 2017, SGL
534 development at higher elevations occurred later in the melt season (Figure 3), despite the daily Ta already falling below
535 0°C. The week prior to July 20th, 2017 (Figure 3a), SMB was mostly positive at elevations greater than 900 m (Figure
536 S4a), however for the five days prior to August 23rd, 2017 (Figure 3b), SMB returned to negative at these higher
537 altitudes (Figure S4b), despite an overall trend towards a positive SMB at lower elevations (Figure S4c). Therefore, not
538 only the local meteorology but also the SMB controls the SGL development, especially at higher elevations.

540 4 Discussion

541 ~~Summer 2016 saw the largest loss of glacier area over the GIS since 2012, which was the standout, record-~~
542 ~~breaking melt year since records began (Hanna et al. 2014a). Summer 2016 also experienced the largest average~~
543 ~~individual SGL size (0.07 km²), second largest total SGL area and second fastest rate of SGL area growth in our four-~~
544 ~~year record. A combination of above average air temperatures, particularly in mid-June and July, and a large amount of~~
545 ~~liquid precipitation during summer was likely responsible for the rapid SGL development and peak in total SGL area in~~
546 ~~late July. Despite the early observation of Ta above freezing in 2017, the earliest in our four-year period, the June 2017~~
547 ~~average Ta was slightly below average. This, combined with the slightly above average July 2017 temperatures, likely~~
548 ~~led to the slower rate of increase in SGL area in 2017 compared to 2016 (Figure 2), and peak in maximum area in early~~
549 ~~August 2017. The thinner snowpack and limited amount of liquid precipitation falling during summer contributed to the~~
550 ~~lower maximum SGL area of 153.26 km² in 2017, compared to 265.39 km² in 2016. In 2018, the spatial distribution of~~
551 ~~SGLs was different to the other three years, with the largest SGL area at elevations between 300 m and 400 m a.s.l~~
552 ~~(Figure 4). Very few SGLs were observed at elevations greater than 900 m, leading to smaller average individual SGL~~
553 ~~area, as no larger lakes at higher elevations were identified (Figure 3). Average individual lake size in 2018 was 0.02~~
554 ~~km², compared to 0.07 km² in 2016, 0.06 km² in 2017 and 2019. A combination of the cooler air temperatures at the~~
555 ~~start of summer (see Section 3.3.1) and thick snowpack led to the delayed onset of SGL development, lower maximum~~
556 ~~altitude of SGLs and lower total SGL area in 2018 (Figure 3). Total SGL area was largest in 2019, even though the~~
557 ~~average size of individual SGLs was the same as in 2017 (0.06 km²). A combination of higher air temperatures, more~~
558 ~~days above freezing and a smaller snowpack at the start of the melt season all contributed to a significantly higher total~~
559 ~~SGL area in 2019 (Figure 4). The peak melt pond area at the start of August 2019 coincides with an air temperature~~
560 ~~peak of 6.9 °C on August 2nd at KPC L, the warmest daily Ta ever recorded here (Figure 5).~~

561 Several years within the last decade have been characterised by high air temperatures and extreme melting,
562 including two within our study period (2016 and 2019). With a projected increase in air temperatures and inland
563 expansion of SGLs into the year 2100 (Leeson et al. 2015; Igneczi et al. 2016), it is important to understand the linkages
564 between different climatic variables and the spatial distribution and temporal evolution of SGLs in the northeast of
565 Greenland. Furthermore, the role of supra glacial melting within the glacial-hydrologic system is in need of further
566 assessment. In a number of studies, enhanced surface melting has contributed to accelerated glacier velocity
567 (Bartholomew et al. 2011; Rathmann et al. 2017), however in other Greenlandic glaciers, especially land-terminating
568 glaciers, ice velocity has decreased with warmer summers (Sundal et al. 2011; Tedstone et al. 2015).

569 The spatial spread of the SGLs on 79 °N Glacier from lower to higher elevations as the melt season progresses
570 is also seen on Leverett Glacier in southwest Greenland (Bartholomew et al. 2011). In southwest Greenland, as the melt
571 season develops, runoff from up-glacier (higher elevation) regions contributes to subglacial discharge at the base of the
572 land-terminating glacier, due to a larger melt area and higher air temperatures (Bartholomew et al. 2011). A similar
573 transport of melt water from surface to base is hypothesised for 79 °N Glacier also. Rathmann et al. (2017) observed a

Moved (insertion) [1]

Formatted: Indent: First line: 1.25 cm

Formatted: Font colour: Red, Not Strikethrough

Formatted: Font colour: Red

Formatted: Font colour: Red, Not Strikethrough

Formatted: Font: Not Bold, Font colour: Red

Moved up [1]: Summer 2016 saw the largest loss of glacier area over the GIS since 2012, which was the standout, record-breaking melt year since records began (Hanna et al. 2014a).

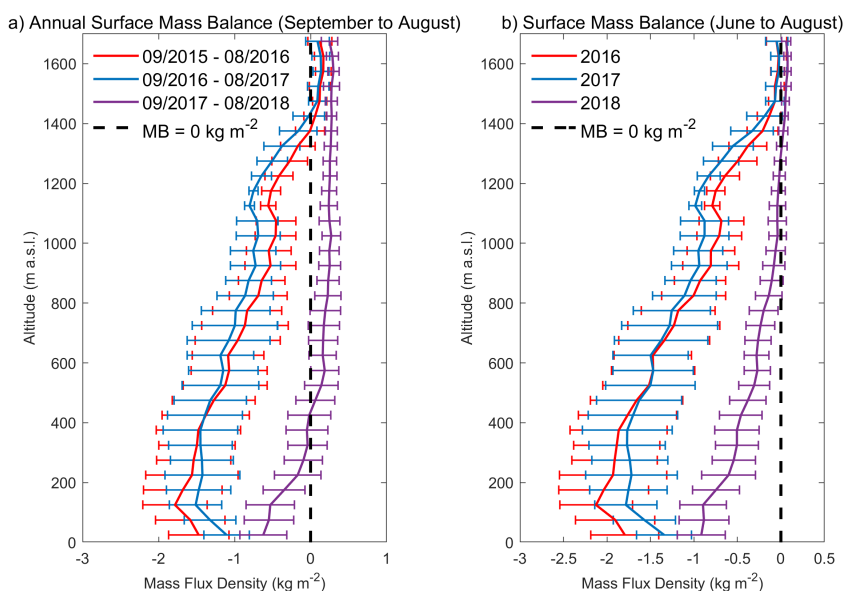
Deleted: More recently, summer 2019 again broke records for melting and temperatures. However, our understanding of the relationship between air temperature and melting is complicated by the development of SGLs and the interaction of other climatic variables.

582 seasonal increase in ice velocity following the particularly warm summer of 2016. An extension of the Rathmann et al.
 583 (2017) study and estimation of the volume of water potentially interacting with the base of the glacier is an important
 584 area of future research.

585 The rapid increase in SGL area over 79 °N Glacier during June in most years was also observed at Petermann
 586 Glacier at 81 °N in the northwest of Greenland. Other similarities in SGL characteristics are found between 79 °N and
 587 Petermann Glaciers, including the spatial distribution of the SGLs and the onset of above-freezing air temperatures at
 588 the start of June (Macdonald et al. 2018). The only summer with overlap between the current study and the Macdonald
 589 et al. (2018) study is 2016. In both locations, this year was characterised by larger total SGL area and warmer than
 590 average air temperatures, highlighting the relationship between SGL development and climatic factors across the north
 591 of Greenland. However, as noted by Macdonald et al. (2018) and observed in the current study in 2018, the low
 592 elevation of these regions dictates that even in cool years, SGLs still form on the lower section of the glaciers.

593 Langley et al. (2016) hypothesized that SGL expansion in the early part of the season is particularly rapid, as
 594 even small changes in air temperature can increase the total lake area. A rapid increase in lake area was seen at the start
 595 of the 2016 and 2019 melt season over 79 °N glacier, however in 2017, late-summer temperatures led to later expansion
 596 of SGLs. The large rate of increase at the start of summer 2016 (Figure 2) is likely skewed by the slightly lower
 597 temporal resolution in 2016 (approximately 3-7 days) compared to the other years (1-2 day). In 2016 and 2017, there
 598 was a lower temporal coverage than the following years as only one Sentinel satellite was in orbit and data quality was
 599 poorer (Hochreuther et al. 2021). However, upon visual inspection of the satellite images, 2016 also saw a rapid
 600 expansion in SGLs, similar to 2019.

601
 602



603
 604 **Figure 10: The annual (a) and summer (JJA) surface mass balance between September 2015 and August 2018, averaged over**
 605 **each altitude in 50m bands. Error bars indicate the standard deviation of SMB for each grid in the respective altitude band.**

606
607 Warmer summer air temperatures alone do not always lead to enhanced melting. For the Shackleton ice shelf
608 in Antarctica, the years with largest SGL area and volume were not always in the same years as the highest summer
609 near-surface air temperatures (Arthur et al. 2020). With only four years of data in the present study, no major
610 conclusions can be drawn on this, however it is clear that precipitation also had an impact on SGL area and
611 development over northeast Greenland. In Buzzard (2018b), the relationship between snowfall and melt pond depth was
612 not simple or linear. A small amount of snowfall will promote melt pond development, as there is more water available
613 at the surface, however a high amount of accumulation can bury the melt pond (especially if the surface has started to
614 freeze towards the end of summer) and reduce melting (Buzzard et al 2018b). We also see evidence of this non-linear
615 response. A combination of a large amount of snowfall prior to the 2018 melt season, and below average summer air
616 temperatures led to a lower total area of SGLs and positive mass balance over the majority of the glacierized area
617 (Figure 9, 10). With a thicker snowpack, it took longer for the SGLs to form, as there was more pore space for water to
618 percolate through before pooling. A thick snowpack was also responsible for a 20-day delay between above-zero air
619 temperatures and runoff in the southwest of Greenland, as the meltwater initially refroze within the cold snowpack
620 (Bartholomew et al. 2011). In the present study, the duration between above-zero air temperatures and melt pond
621 development varies from 7 to 14 days at KPC_L and 1 to 16 days at KPC_U. The shortest duration was observed in
622 2019, which had the thinnest snowpack of the four-year period. Similar conclusions were found for Tibetan glaciers
623 (Mölg et al. 2012) and Shackleton ice shelf in the Antarctic (Arthur et al. 2020).

624 Conversely, the year with the smallest snowfall amount (2018-2019 accumulation season) was not followed by
625 the summer with the fewest melt ponds. However, the much higher air temperatures and late summer freeze up of SGLs
626 in 2018 played a bigger role. Summer 2016 saw the second largest total SGL area and spatial distribution of SGLs. This
627 year also saw a large amount of precipitation fall as rainfall in summer. Rainfall is additional liquid for the surface of
628 the glacier, provides heat to the snowpack and refreezes into solid ice lenses which preconditions the glacier surface for
629 further SGL development (Machguth et al. 2016). Rainfall associated with summer storms has been linked to extreme
630 melting events in southern Greenland by Oltmanns et al. (2019) and enhanced ice velocity in western Greenland by
631 Doyle et al. (2015). Similarly, Tedesco and Fettweis (2020) concluded that low snow accumulation was also partly
632 responsible for the extensive melting along much of the coast of Greenland in 2019.

633 Relationships between large-scale temporal and spatial anomalies within the atmosphere, termed
634 teleconnections, have been found to influence the climate and mass balance of Greenland (Tedesco et al. 2013; Lim et
635 al. 2016). With only four years of data in the current study, we are unable to draw conclusions about the role of
636 teleconnections in the development of SGLs, however there is evidence that combinations of teleconnection indices
637 play a role in the near-surface climate and therefore SGL development in the northeast of Greenland. In 2016 and 2019,
638 the average summer (JJA) North Atlantic Oscillation (NAO) index was strongly negative (-1.36 for 2016, -1.23 for
639 2019) (see Supplementary material for teleconnection data). Simultaneously, both the summer East Atlantic (EA) index
640 and the Greenland Blocking Index (GBI) were strongly positive in both of these years. In summer 2016, the EA (GBI)
641 summer average was 1.44 (1.73). Similarly, in 2019 the JJA average EA index (GBI index) was 1.1 (2.26). This
642 combination of strong negative NAO and strong positive EA also occurred in both summer 2010 and 2012, when
643 extensive melting was observed over the GIS (Lim et al. 2016). In terms of teleconnections, the biggest differences
644 between 2016/2019 and the 2017/2018 summers was the NAO and GBI summer indices. In 2017 the NAO index was
645 positive in June and July. In 2018 the summer NAO index was strongly positive (1.74), with all summer months
646 observing a positive NAO signal. The GBI for summer 2017 and 2018 was weakly negative (-0.03) and negative (-0.57)
647 respectively. In terms of the teleconnection indices evaluated here, summer 2017 appears to be the intermediate or

648 transition year between a particularly strong negative NAO in 2016 and a strong positive NAO in 2018. A decreasing
649 trend in summer NAO since 1981 has been previously identified and is believed to be partly responsible for record-
650 breaking warm temperatures over Greenland in the most recent decade (Hanna et al. 2014).

651 The relationship between teleconnections and precipitation is more complicated and is often only significant in
652 the southern part of Greenland where the majority of the precipitation falls. Bjork et al. (2018) identified a positive
653 relationship between NAO and precipitation in eastern Greenland: there is more precipitation during positive NAO
654 years. The year with the largest cumulative precipitation amounts was the 2017-2018 accumulation season, which was
655 also characterised by a strong positive NAO index. However, the relationship between NAO and precipitation for NE
656 Greenland cannot be assessed with certainty in this study.

657 Although we present only four years of results here and previous studies in this region are sparse, we are
658 confident that SGLs are a persistent feature in the NEGIS and 79 °N region. Sundal et al. (2009) observed SGLs
659 between 2003 and 2007 using MODIS data. With the availability of ~~very high-resolution (10 m) Sentinel data (10 m~~
660 ~~resolution)~~, the SGL areas are less erroneous than previously stated using lower-resolution MODIS data (250 m)
661 (Hochreuther et al. 2021). There is an increase in the maximum altitude of SGL detection between the early 2000's
662 study of Sundal et al. (2009) (1200 m a.s.l) and the results presented here (1600 m a.s.l). The lakes at these higher
663 elevations are larger and therefore would have been detected by the MODIS data in the Sundal et al. (2009) study, were
664 they present. Therefore, it is likely that maximum lake altitude has increased over time.

665 This is not surprising given an increasing air temperature trend of 0.8 °C decade⁻¹ over 79 °N Glacier (Turton et
666 al. 2019), and model suggestions of inland expansion in this area into the 21st century (Ignéczki et al. 2016). Leeson et al.
667 (2015) concluded that maximum lake altitude could reach up to 2221 m a.s.l with RCP 8.5 future projections. Although
668 there are a number of assumptions made in our comparison to Sundal et al. (2009), it is possible that inland expansion
669 of lakes is occurring under increased air temperatures in this region.

670 Under certain high-melt years, surface rivers have been observed for a number of northern Greenland glaciers,
671 including 79 °N (Bell et al. 2017). While we do not consider meltwater channels in our analysis and focus only on
672 SGLs, a number of linear features similar to rivers are clearly visible in the Sentinel data (Figure S1). This highlights
673 that more liquid water is likely present on and within the glacier than discussed here. There is even some evidence of
674 the persistence of liquid water in melt lakes during the winter season on 79 °N Glacier (Schröder et al. 2020). It is
675 hypothesised that lakes beneath the surface were formed in particularly warm years (such as 2019) and then
676 subsequently covered by a thin ice lens or snow (Schröder et al. 2020).

677 Estimates of the SGL volume are not provided in this study, which is unusual for these types of studies (e.g
678 Pope et al. 2016., Arthur et al. 2020). We hypothesise that SGLs in this region are much deeper than those observed in
679 the west of Greenland (on the order of 0-10 m). Neckel et al. (2020) recorded the depth of an SGL on the 79 °N Glacier,
680 which, at the edge of the lake, had a depth of 10.8 m. The same lake drained suddenly in September 2017, and analysis
681 of the height difference from a full to empty lake using DEMs revealed a subsidence of 50 m in the centre of the lake
682 (Neckel et al. 2020). Therefore, applying the same albedo-depth calculation to the lakes in northeast Greenland as in
683 western Greenland would largely underestimate the volumes. In-situ observations of these lakes are required to
684 calculate depth and volume with a different albedo-depth coefficient. Fieldwork is planned for this region, to observe
685 the depth of SGLs.

686

687 5 Conclusions

688 In this study we provide a multi-year analysis of the area of SGLs over the 79 °N Glacier (northeast Greenland) and
689 investigate the atmospheric and topographic controls of the evolution of the lakes. SGLs have been automatically

Formatted: Strikethrough

Formatted: Font colour: Red

690 detected using Sentinel-2 data, from 2016 to 2019. The melt detection algorithm implemented here and developed by
691 Hochreuther et al. (2021) is automated, meaning that this work can be continued in the future to analyse a long-term
692 time series of SGL evolution. Our findings would ideally now be expanded to include volume estimates and to model
693 the surface and subglacial hydrology to provide an estimate of the volume of fresh water entering the ocean.

694 Whilst the SGL location is primarily determined by topographic depressions and the slope of the ice sheet, the
695 occurrence of lakes within these depressions relies on the local meteorology and SMB. Similar to the spatial
696 distribution, the maximum size of individual lakes is controlled by topography. At higher elevations, larger lakes form
697 due to a lower slope angle (Figure 4). The larger total SGL areas in 2016 and 2019 were due to lakes developing at
698 higher elevations than in 2017 and 2018, as opposed to individual lakes becoming larger. SGLs refreeze and melt in the
699 same locations above the grounding line each year, but maximum inland expansion of the lakes depends on climatic
700 conditions.

701 The two key climatic variables controlling the development of the SGLs are air temperature and snowfall.
702 Below average air temperatures and high snowfall accumulation prior to the melt season of 2018 contributed to reduced
703 lake extent, a reduced amplitude in the seasonal cycle of lake evolution and late season freeze up of the SGLs. These
704 climatic conditions led to a largely positive mass balance at all altitudes except the very lowest lying regions.
705 Conversely, in the prior two years, surface mass balance was negative for a large portion of 79 °N Glacier and the
706 surrounding area. Largely this was driven by the above average air temperature, evident in both the in-situ AWS data
707 (Figure 5) and in the regional atmospheric modelling output (Figure 6, 7). The duration between onset of above-zero air
708 temperatures and SGL development varies between 1 and 16 days, depending on the year and elevation. The snowpack
709 thickness prior to the warm air temperatures likely also has an influence on this duration.

710 The role of clouds in melt production over the Greenland Ice Sheet is often studied (e.g Bennartz et al. 2013).
711 Within the four years, the warm summer of 2016 coincided with a positive bias in SWin and a reduction in cloud cover,
712 however the warm June of 2019 was characterised by negative biases in SWin. Similarly, the relatively cool summer of
713 2018 was characterised by positive anomalies in SWin and higher than average cloud cover in June. With just four
714 years of data in the current study, no clear conclusions can be drawn on the role of clouds on the development of SGLs
715 in this region.

716 Whilst 2019 was record breaking in terms of melt over much of the Greenland ice sheet, in fact second only to
717 2012 (Tedesco and Fettweis, 2020), the summer of 2016 was only warm and extreme in the northeast region. The
718 extreme summer temperatures led to extensive SGL formation over the 79 °N Glacier, as well as subsequent ice
719 velocity acceleration (Rathmann et al. 2017). Similarly, 2019 was not a record-breaking melt year in the northeast of
720 Greenland, and at lower elevations, the number of melt days (TSK_{melt}) and the duration of melting was less than in other
721 years. This highlights the importance of regional studies of extreme melting, as well as the Greenland ice sheet-wide
722 studies.

723 There is some evidence of inland expansion of lakes between the Sundal et al. (2009) study, which looked at
724 SGLs between 2003 and 2007, and the present findings from 2016 to 2019. The highest elevation of SGLs in the early
725 2000's was 1200 m a.s.l, whereas in the late 2010's, SGLs above 1600 m a.s.l were observed. This is in line with global
726 climate model projections for inland expansion of SGLs and the ablation zone under climate change (Ignéczi et al.
727 2016). The northeast of Greenland is expected to undergo the largest changes in SMB and SGLs by 2100 and therefore
728 should feature in future atmosphere-glaciohydrology studies.

729

730 **6 Data Availability**

731 The daily average surface mass balance data is available at: <https://doi.org/10.5281/zenodo.4434259>. For higher
732 temporal resolution see Blau et al. (2021). The daily average PWRF data is available at:
733 <https://doi.org/10.17605/OSF.IO/53E6Z>. For higher temporal resolutions see Turton et al. (2020). Lake outline
734 polygons and cloud masks are available on request and are currently being uploaded to Pangaea Data Centre, pending a
735 DOI.

736
737 **7 Author Contribution**
738 J.V.T wrote the manuscript and conducted the climatological analysis. P.H developed and applied the automatic
739 detection algorithm for the SGLs and assisted in discussing the results. N.R assisted in the development of the algorithm
740 and writing the manuscript. M.T.B. conducted the SMB modelling and analysis.

741
742 **8 Competing Interests**
743 The authors declare no conflict of interest.

744
745 **9 Acknowledgements**
746 We are grateful to the European Space Agency (ESA) for providing the Sentinel-2 data and to the Greenland and
747 Denmark Geological Survey (GEUS) for maintaining the AWS and providing the data. We acknowledge the German
748 Federal Ministry for Education and Research (BMBF) for funding this work as part of the GROCE project (Greenland
749 Ice Sheet/Ocean Interaction) (Grant 03F0778F and 03F0855F). We also thank the High-Performance Computing Centre
750 (HPC) at the University of Erlangen-Nürnberg's Regional Computation Centre (RRZE) for their support and resources.
751 We also thank two anonymous reviewers and the editor Dr Stef Lhermitte for their insights and feedback.

752
753 **10 References**
754 Arthur, J.F., Stokes, C.R., Jamieson, S.S.R., Carr, J.R. and Leeson, A.A.: Distribution and seasonal evolution of
755 supraglacial lakes on Shackleton Ice Shelf, East Antarctica. *The Cryosphere*, 14 (11), 4103-4120, doi:10.5194/tc-14-
756 4103-2020, 2020.
757 Bartholomew, I., Nienow, P., Sole, A., Mair, D., Cowton, T., Palmer, S. and Wadham, J.: Supraglacial forcing of
758 subglacial drainage in the ablation zone of the Greenland ice sheet. *Geophysical Research Letters*, 38, L08502,
759 doi:10.1029/2011GL047063, 2011.
760 Blau, M.T., Turton, J.V., Mölg, T. and Sauter, T.: Surface mass and energy balance estimates of the 79N Glacier
761 (Nioghalvfjærdssjøen, NE Greenland) modeled by linking COSIPY and Polar WRF. *J. Glaciology*. 1-15,
762 doi:10.1017/jog.2021.56, 2021.
763 Bell, R.E., Chu, W., Kingslake, J., Das, I., Tedesco, M., Tinto, K.J., Zappa, C.J., Frezzotti, M., Boghosian, A., Sang
764 Lee, W.: Antarctic ice shelf potentially stabilized by export of meltwater in surface river, *Nature*, 544, 344-348,
765 doi:10.1038/nature22048, 2017.
766 Bonne, J-L., Steen-Larsen, H.C., Risi, C., Werner, M., Sodemann, H., Lacour, J-L., Fettweis, X., Cesana, G., Delmotte,
767 M., Cattani, O., Vallelonga, P., Kjae, H.A., Clerbaux, C., Sveinbjörnsdóttir, A.E. and Masson-Delmotte, V.: The
768 summer 2012 Greenland heat wave: in situ and remote sensing observations of water vapor isotopic composition during
769 an atmospheric river event. *JGR: Atmospheres*, 120, (7), 2970-2989, doi:10.1002/2014JD022602, 2015.
770 Buzzard, S.C., Feltham, D.L. and Flocco, D.: A mathematical model of melt lake development on an ice shelf. *J.*
771 *Advances in Modeling Earth Systems*, 10 (2), 262-283, doi:10.1002/2017MS001155, 2018a

772 Buzzard, S.C., Feltham, D. and Flocco, D.: Modelling the fate of surface melt on the Larsen C ice shelf. *The*
773 *Cryosphere*, 12 (11), 3565-3575, doi:10.5194/tc-12-3565-2018, 2018b.

774 Das, S.B., Joughin, I., Behn, M.D., Howat, I.M., King, M.A., Lizarralde, D. and Bhatia, M.P.: Fracture propagation to
775 the base of the Greenland Ice Sheet during supraglacial lake drainage. *Science*, 320 (5877), 778-781,
776 doi:10.1126/science.1153360, 2008.

777 Doyle, S.H., Hubbard, A., van de Wal, R.S.W., Box, J.E... Hubbard, B.: Amplified melt and flow of the Greenland ice
778 sheet driven by late-summer cyclonic rainfall. *Nat Geosci.* 8, 647-653, doi:10.1038/ngeo2482, 2015

779 Flowers, G.: Hydrology and the future of the Greenland Ice Sheet. *Nature Comms.* 9, 2729, doi:10.1038/s41467-018-
780 05002-0, 2018.

781 Hanna, E., Fettweis, X., Mernild, S.H., Cappelen, J., Ribergaard, M.H., Shuman, C.A., Steffen, K., Wood, L. and Mote,
782 R.L.: Atmospheric and oceanic climate forcing of the exceptional Greenland ice sheet surface melt in summer 2012. *Int.*
783 *J. Climatology*, 34, 1022-1037, doi:10.1002/joc.3743, 2014a

784 Hanna, E., Cropper, T.E., Jones, P.D., Scaife, A.A. and Allan, R.: Recent seasonal asymmetric changes in the NAO (a
785 marked summer decline and increased winter variability) and associated changes in the AO and Greenland Blocking
786 Index. *Int. J. climatology*, 35 (9), 2540- 2554, doi:10.1002/joc.4157, 2014b

787 Hildebrandsson, H.H.: Quelques recherches sur les centres d'action de l'atmosphere, I-IV. *Kungliga Svenska*
788 *Vetenskaps-Akademiens Handlingar*, 29 (3), 36. 1897.

789 Hines, K. M., Bromwich, D. H., Bai, L., Bitz, C. M., Powers, J. G., Manning, K. W.: Sea Ice
790 Enhancements to Polar WRF*. *Mon. Weather Rev.*, 143(6), 2363-2385, doi:10.1175/MWR-
791 D-14-00344.1, 2015.

792 Hochreuther, P., Neckel, N., Reimann, N., Humbert, A. and Braun, M.: Fully automated detection of supra-glacial lake
793 area for northeast Greenland using Sentinel-2 time series. *Remote sensing*, 13(2), 205, doi:10.3390/rs13020205, 2021.

794 Howat, I.M., Negrete, A. and Smith, B.E.: The Greenland Ice Mapping Project (GIMP) Land Classification and Surface
795 Elevation Data Sets. *Cryosphere* 2014, 8, 1509–1518, doi: 10.5194/tc-8-1509-2014.

796 Igneczi, A., Sole, A.J., Livingstone, S.J., Leeson, A.A., Fettweis, X., Selmes, N., Gourmelen, N. and Briggs, K.:
797 Northeast sector of the Greenland ice sheet to undergo the greatest expansion of supraglacial lakes during the 21st
798 century. *Geophysical research letters*. 43 (18), 9729-9738, doi:10.1002/2016GL070338, 2016.

799 Khan, S. A., Kjær, K. H., Bevis, M., Bamber, J. L., Wahr, J., Kjeldsen, K. K., Bjørk, A.A., Korsgaard, N.J., Stearns,
800 L.A., van den Broeke, M.R, Liu, L., Larsen, N.K. and Muresan, I. S: Sustained mass loss of the northeast Greenland
801 ice sheet triggered by regional warming. *Nature Climate Change*, 4(4), 292–299, doi:10.1038/nclimate2161, 2014.

802 Kingslake, J., Ng, F. and Sole, A.: Modelling channelized surface drainage of supraglacial lakes. *J. Glaciology*, 61,
803 doi:10.3189/2015JoG14J158, 2015

804 Krieger, L., Floricioiu, D. and Neckel, N.: Drainage basin delineation for outlet glaciers of northeast Greenland
805 based on Sentinel-1 ice velocities and TanDEM-X elevations. *Remote sensing of the environment*, 237, 111483,
806 doi:10.1016/j.rse.2019.111483, 2020.

807 Lampkin, D.J. and VanderBerg, J.: A preliminary investigation of the influence of basal and surface topography on
808 supraglacial lake distribution near Jakobshavn Isbrae, western Greenland. *Hydrological Processes*, 25, 3347-3355,
809 doi:10.1002/hyp.8170, 2011.

810 Langley, E.S., Leeson, A.A., Stokes, C.R., Jamieson, S.S.R.: Seasonal evolution of supraglacial lakes on an East
811 Antarctic outlet glacier, *Geophys. Res. Lett.*, 43, doi:10.1002/2016GL069511, 2016.

812 Leeson, A.A., Shepherd, A., Briggs, K., Howat, I., Fettweis, X., Morlighem, M. and Rignot, E.: Supraglacial lakes on
813 the Greenland ice sheet advance inland under warming climate. *Nature Climate Change*, 5, 51-55,
814 doi:10.1038/nclimate2463, 2015.

815 Leeson, A.A., Forster, E., Rice, A., Gourmelen, N., van Wessem, J.M.: Evolution of supraglacial lakes on the Larsen B
816 ice shelf in the decades before it collapsed, *Geophys. Res. Lett.*, 47, doi:10.1029/2019GL085591, 2020.

817 Lim, Y-K., Schubert, S.D., Nowicki, S.M.J., Lee, J.N., Molod, A.M., Cullather, R.I., Zhao, B. and Velicogna, I.:
818 Atmospheric summer teleconnections and Greenland Ice Sheet surface mass variations: insights from MERRA-2.
819 *Environmental Research Letters*, 11 (2), 024002, doi:10.1088/1748-9326/11/2/024002, 2016.

820 Luckman, A., Elvidge, A., Jansen, D., Kulesa, B., Kuipers Munneke, P., King, J. and Barrand, N.E.: Surface melt and
821 ponding on Larsen C ice shelf and the impact of foehn winds. *Antarctic Science*, 26 (6), 625-635,
822 doi:10.1017/S0954102014000339, 2014.

823 Luthje, M., Pedersen, L.T., Reeh, N. and Greuell, W.: Modelling the evolution of supraglacial lakes on the West
824 Greenland ice-sheet margin. *J. Glaciology*, 52 (179), 608-618, doi:10.3189/172756506781828386, 2006.

825 Macdonald, G.J., Banwell, A. and MacAyeal.: Seasonal evolution of supraglacial lakes on a floating ice tongue,
826 Petermann Glacier, Greenland. *Annals of Glaciology*, 59 (76pt1), 56-65, doi:10.1017/aog.2018.9, 2018.

827 MacFerrin, M., Machguth, H., van As, D., ... Abdalati, W.: Rapid expansion of Greenland's low permeability ice slabs.
828 *Nature*, 573, 403-407. Doi:10.1038/s41586-019-1550-3, 2019.

829 Machguth, H., MacFerrin, M., van As, D., Box, J.E., Charalampos, C., Colgan, W., Fausto, R.S., Meijer, H, Mosley-
830 Thomposon, E. and van de Wal, R.S.W.: Greenland meltwater storage in firn limited by near-surface ice formation. *Nat.*
831 *Clim. Change*, 6, 390-393, doi:10.1038/nclimate2899, 2016.

832 Malinka, A., Zege, E., Istomina, L., Heygster, G., Spreen, G., Perovich, D. and Polashenski, C.: Reflective properties
833 of melt ponds on sea ice. *The Cryosphere*, 12 (6), 1921-1937, doi:10.5194/tc-12-1921-2018, 2018.

834 Mayer, C., Schaffer, J., Hattermann, T., Floricioiu, D., Krieger, L., Dodd, P. A., ... Schannwell, C: Large ice
835 loss variability at Nioghalvfjærdssjøorden Glacier, Northeast Greenland, *Nature Comms*, 9(1), 2768,
836 doi:10.1038/s41467-018-05180-x, 2018.

837 Mölg, T., Maussion, F., Yang, W. and Scherer, D: The footprint of Asian monsoon dynamics in the mass and energy
838 balance of a Tibetan glacier, *The Cryosphere*, 6, 1445-1462, doi:10.5194/tc-6-1445-2012, 2012.

839 Mougint, J., Rignot, E., Scheuchl, B., Fenty, I., Khazendar, A., Morlighem, M., Buzzi, A. and Paden, J.: Fast retreat
840 of Zachariae Isstrøm, northeast Greenland. *Science*, 350 (6266), 1357-1361, doi:10.1126/science.aac7111, 2015.

841 Neckel, N., Zeising, O., Steinhage, D., Helm, V. and Humbert, A.: Seasonal observations at 79°N Glacier
842 (Greenland) from remote sensing and in situ measurements. *Frontiers Earth Sci.*, 8 (142),
843 doi:10.3389/feart.2020.00142, 2020.

844 Noël, B., van de Berg, W.J., Lhermitte, S. and van den Broeke, M.: Rapid ablation zone expansion amplifies north
845 Greenland mass loss. *Science Advances*, 5 (9), eaaw0123, doi:10.1126/sciadv.aaw0123, 2019.

846 Oltmanns, M., Straneo, and Tedesco, M.: Increased Greenland melt triggered by large scale, year-round cyclonic
847 moisture intrusions. *The Cryosphere*, 13 (3), 815-825, doi:10.5194/tc-13-815-2019, 2019.

848 Perovich, D.K., Grenfell, T.C., Light, B. and Hobbs, P.V.: Seasonal evolution of the albedo of multiyear Arctic sea
849 ice, *JGR: Oceans*, 107 (C10), 20-1 – 20-13, doi:10.1029/2000JC000438, 2002.

850 Polar Weather Research and Forecasting Model, developed by Ohio State University, available from:
851 <http://polarmet.osu.edu/PWRF/>, last accessed: July 29 2019.

852 Pope, A., Scambos, T.A., Moussavi, M., Tedesco, M., Willis, M., Shean, D. and Grigsby, S.: Estimating supraglacial
853 lake depth in West Greenland using Landsat 8 and comparison with other multispectral methods, *The Cryosphere*,

854 10 (1), 15-27, doi:10.5194/tc-10-15-2016, 2016

855 Rathmann, N.M., Hvidberg, C.S., Solgaard, A.M., Grinsted, A., Gudmundsson, H., Langen, P.L., Nielsen, K.P. and
856 Kusk, A.: Highly temporally resolved response to seasonal surface melt of the Zachariae and 79N outlet glaciers in
857 northeast Greenland. *Geophysical Research Letters*, 44 (19), 9805-9814, doi:10.1002/2017GL074368, 2017.

858 Sauter, T., Arndt, A. and Schneider, C.: COSIPY v1.3 – an open-source coupled snowpack and icesurface energy and
859 mass balance model. *Geosci. Model Dev.* 13, 5645-5662, doi:10.5194/gmd-13-5645-2020, 2020

860 Schröder, L., Neckel, N., Zindler, R. and Humbert, A.: Perennial Supraglacial Lakes in Northeast Greenland Observed
861 by Polarimetric SAR. *Remote sensing*, 12, 2798, doi:10.3390/rs12172798, 2020.

862 Smith, L., Yang, K., Pitcher, L.H., Overstreet, B.T., Chu, V.W., Rennermalm, A.K., Ryan, J.C., ...Behar, A.E: Direct
863 measurements of meltwater runoff on the Greenland ice sheet surface, *PNAS*, 114 (50), E10622-E10631,
864 doi:10.1073/pnas.1707743114, 2015.

865 Sundal, A.V., Shepherd, A., Nienow, P., Hanna, E., Palmer, S. and Huybrechts, P.: Evolution of supra-glacial lakes
866 across the Greenland Ice Sheet. *Remote sensing of Environment*, 113, 2164-2171, doi:10.1016/j.rse.2009.05.018, 2009.

867 Sundal, A.V., Shepherd, A., Nienow, P., Hanna, E., Palmer, S. and Huybrechts, P.: Melt-induced speed-up of Greenland
868 ice sheet offset by efficient subglacial drainage. *Nature*, 469, 520-524, doi:10.1037/nature09740, 2011.

869 Tedesco, M., Lütke, M., Steffen, K., Steiner, N., Fettweis, X., Willis, I., Bayou, N. and Banwell, A.: Measurement and
870 modeling of ablation of the bottom of supraglacial lakes in western Greenland. *Geophysical Research Letters*, 39,
871 L02502, doi:10.1029/2011GL049882, 2012.

872 Tedesco, M., Fettweis, X., Mote, T., Wahr, J., Alexander, P., Box, J. E., and Wouters, B: Evidence and analysis of
873 2012 Greenland records from spaceborne observations, a regional climate model and reanalysis data, *The*
874 *Cryosphere*, 7(2), 615–630, doi:10.5194/tc-7-615-2013, 2013.

875 Tedesco, M. and Fettweis, X.: Unprecedented atmospheric conditions (1948-2019) drive the 2019 exceptional
876 melting season over the Greenland ice sheet. *The Cryosphere*, 14 (4), 1209-1223, doi:10.5194/tc-14-1209-2020,
877 2020.

878 Tedstone, A.J., Nienow, P.W., Gourmelen, N., Dehecq, A., Goldberg, D. and Hanna, E.: Decadal slowdown of a
879 land-terminating sector of the Greenland Ice Sheet despite warming. *Nature*, 526, 692-695,
880 doi:10.1038/nature15722, 2015.

881 Turton, J. V., Mölg, T. & Van As, D: Atmospheric Processes and Climatological Characteristics of the 79N Glacier
882 (Northeast Greenland), *Mon. Weather Rev.*, 147(4), 1375–1394, doi:10.1175/MWR-D-18-0366.1, 2019a.

883 Turton, J. V., Mölg, T and Collier, E: NEGIS_WRF model output, Open Science Framework Repository, last accessed
884 October 1 2019, doi: /10.17605/OSF.IO/53E6Z, 2019b.

885 Turton, J.V., Mölg, T and Collier, E: High-resolution (1 km) Polar WRF output for 79°N Glacier and the northeast of
886 Greenland from 2014 to 2018, *Earth System Science Data*, 12, 1191-1202, doi:10.5194/essd-12-1191-2020, 2020.

887 van As, D., and Fausto, R: Programme for Monitoring of the Greenland Ice Sheet (PROMICE): first temperature
888 and ablation records. *Geolog. Survey Denmark Greenland Bulletin*, 23, 73–76, doi:10.34194/geusb.v23.4876, 2011.

889 Vijay, S., Khan, S.A., Kusk, A., Solgaard, A.M., Moon, T. and Bjørk, A.A.: Resolving seasonal ice velocity of 45
890 Greenlandic glaciers with very high temporal details. *Geophysical Research Letters*, 46 (3), 1485-1495,
891 doi:10.1029/2018GL081503, 2019.

892 Wang, C., Graham, R.M., Wang, K., Gerland, S. and Granskog, M.A.: Comparison of ERA5 and ERA-Interim near
893 surface air temperature, snowfall and precipitation over Arctic sea ice: effects on sea ice thermodynamics and evolution.
894 *The Cryosphere*, 13, 1661-1679, doi:10.5194/tc-13-1661-2019, 2019

895 Yang, K., Smith, L.C., Fettweis, X., Gleason, C.J., Lu, Y. and Li, M: Surface meltwater runoff on the Greenland ice
896 sheet estimated from remotely sensed supraglacial lake infilling rate. *Remote Sensing of Environment*, 234, 111459,
897 doi:10.1016/j.rse.2019.111459, 2019.
898 Zwally, H.J., Abdalati, W., Herring, T., Larson, K., Saba, J. and Steffen, K.: Surface melt-induced acceleration of
899 Greenland ice sheet flow. *Science*, 297 (5579), 218-222, doi:10.1126/science.1072708, 2002.
900
901